



Identifying Cross-individual Correspondences of 3-hinge Gyri

Tuo Zhang^{a,*}, Ying Huang^a, Lin Zhao^{a,b}, Zhibin He^a, Xi Jiang^c, Lei Guo^a, Xiaoping Hu^d, Tianming Liu^b



^a School of Automation, Northwestern Polytechnical University, Xi'an, China

^b Cortical Architecture Imaging and Discovery Lab, Department of Computer Science and Bioimaging Research Center, The University of Georgia, Athens, GA, USA

^c School of Life Science and Technology, MOE Key Lab for Neuroinformation, University of Electronic Science and Technology of China, Chengdu, China

^d Department of Bioengineering, University of California Riverside, Riverside, CA, USA.

ARTICLE INFO

Article history:

Received 26 September 2019

Revised 4 April 2020

Accepted 7 April 2020

Available online 13 April 2020

Keywords:

Gyrus hinge

Structural connectivity

Cortical folding pattern

Cross-subject correspondence

ABSTRACT

Human brain alignment based on imaging data has long been an intriguing research topic. One of the challenges is the huge inter-individual variabilities, which are pronounced not only in cortical folding patterns, but also in the underlying structural and functional patterns. Also, it is still not fully understood how to link the cross-subject similarity of cortical folding patterns to the correspondences of structural brain wiring diagrams and brain functions. Recently, a specific cortical gyrus folding pattern was identified, which is the conjunction of gyri from multiple directions and termed a "gyral hinge". These gyral hinges are characterized by the thickest cortices, the densest long-range fibers, and the most complex functional profiles in contrast to other gyri. In addition to their structural and functional importance, a small portion of 3-hinges found correspondences across subjects and even species by manual labeling. However, it is unclear if such cross-subject correspondences can be found for all 3-hinges, or if the correspondences are interpretable from structural and functional aspects. Given the huge variability of cortical folding patterns, we proposed a novel algorithm which jointly uses structural MRI-derived cortical folding patterns and diffusion-MRI-derived fiber shape features to estimate the correspondences. This algorithm was executed in a group-wise manner, whereby 3-hinges of all subjects were simultaneously aligned. The effectiveness of the algorithm was demonstrated by higher cross-subject 3-hinges' consistency with respect to structural and functional metrics, when compared with other methods. Our findings provide a novel approach to brain alignment and an insight to the linkage between cortical folding patterns and the underlying structural connective diagrams and brain functions.

© 2020 Elsevier B.V. All rights reserved.

1. Introduction

Brain alignment is one of the important approaches to enable cross-subject and cross-group comparative studies, which further facilitates mapping studies of brain structure and function as well as their relationships, and further improve the understanding of the brain mechanisms (Talairach and Tournoux, 1988; Mazziotta et al., 2001; Lancaster et al., 2007; Derrfuss and Mar, 2009). One of the important goals of brain alignment is to match functional regions across subjects. However, due to the infeasibility in some clinical scenarios (e.g., Epstein et al., 2007; Raschle et al., 2012) and the prohibitive cost, functional data, such as functional MRI data, are not widely available. Therefore, brain alignment has largely relied on anatomical features. While many automated volume reg-

istration methods have been developed and successfully used to align brain structures (Thompson and Toga, 1996; Shen and Davatzikos, 2002; Avants and Tustison, 2009; Greve and Fischl, 2009; Klein et al., 2009), surface registration methods are usually preferred for cortical area alignment on 2D manifolds (Van Essen et al., 1998; Fischl et al., 1999a, 1999b; Van Essen, 2004; Goebel et al., 2006). In these surface registration methods, cortical folding patterns are aligned because they are demonstrated to predict cortical areas, especially the primary ones (Fischl et al., 2007; Hinds et al., 2008) and even improve the alignment of functional areas (Frost and Goebel, 2012; Van Atteveldt et al., 2004). However, the predictive accuracy drops dramatically on cognitive and association cortex of higher orders (Fischl et al., 2007), because of higher inter-individual variabilities of their cortical folding patterns. On these cortical regions, a mismatching between brain function and cortical folds was reported (Amunts et al., 2000; Fischl et al., 2007; Hinds et al., 2008; Glasser and Van Essen, 2011; Frost and Goebel,

* Corresponding Author. #127, West Youyi Road, Xi'an, Shaanxi, China, 710072.
Tel.: (+86)17795741808

E-mail address: tuzhang@nwpu.edu.cn (T. Zhang).

2012). Therefore, the folding pattern matching could only yield a sub-optimal solution to the brain function alignment.

An explanation to the fold matching inaccuracy and the disparity between brain function and its cortical folding appearance is that the previous brain anatomy-function mapping was at a coarse level. For example, cortical folds were usually depicted by metrics, such as curvature and gyration index (Zilles et al., 1989). These metrics are at a very local scale and not robust to noise, such that they were usually used on a large cortical patch to give an overall and implicit measurement of its complexity (Fischl et al., 2007) and could not necessarily guarantee an accurate correspondence (Pantazis et al., 2010). A more explicit descriptor of cortical folds is the gyral-sulcal patterns, which were usually used as cortical landmarks because their shapes have been linked to cytoarchitectonic boundaries of the cortex. Some works have succeeded in using sulcal fundi as landmarks to improve the performance of cortex alignment (Desai et al., 2005; Van Essen, 2005; Pantazis et al., 2010). Such an improvement could be attributed to the better competence of gyral-sulcal patterns at decomposing a relatively large cortex to more specific, basic and depictive morphological components.

In addition to the classic gyral-sulcal cortical landmarks, several efforts were found to define cortical folding landmarks at a finer resolution. For example, in Régis et al., 2005, the authors defined an indivisible unit, "sulcal root". They found that these units were organized as a scheme that was stable across individuals at the fetal stage. Another example is "sulcal pits" (Lohmann et al., 2007), which are the deepest parts defined on sulci. These sulcal pits were also demonstrated to exhibit fewer inter-individual variabilities. These studies showed that conventional gyral-sulcal landmarks are far from the limits of cortical folding representation. A meaningful cortical landmark at a finer resolution could decompose cortical folds to more depictive units and improve the alignment of brain anatomy and function.

Following this trajectory, we recently characterized a unique cortical folding pattern, which is the conjunction of gyri from multiple directions and is termed a gyral hinge (see their locations highlighted by yellow bubbles in Fig. 1). As gyral hinges with more than three gyral spikes are rarely seen, the major interest in this work is focused on those with three gyral spikes, and we use 3-hinge to denote it in the following sections. These 3-hinges are of a great number (especially on human brains) and scattered on the entire cortex. They are characterized by the thickest cortex, the densest long-range fibers in contrast to other gyral counterparts and sulcal regions (Ge et al., 2017). They were also found to be simultaneously involved in more global functional networks during resting state and a variety of task performances than other folding patterns (Jiang et al., 2015). We recently developed an automated algorithm to extract a novel cortical folding organization system, termed gyral net (white curves in Figs. 1 & 2). This system is defined on gyral crest and is closed and self-contained (Chen et al., 2017), in which 3-hinges link their neighbor gyral crestlines (see the spatial relation between the gyral net and 3-hinges in Fig. 1). Altogether, the anatomical, structural and functional importance of 3-hinges endorses them with critical roles as possible cortical hubs of brains (Jiang et al., 2015; Ge et al., 2017; Zhang et al., 2019), and thus provides a unique window to study the linkage between the different aspects of brains. More importantly, a small group of 3-hinges have been demonstrated to have cross-subject and even cross-species correspondence by a manual labeling work (Li et al., 2017) regarding their consistent folding morphology and fiber connective patterns. All these characteristics of 3-hinges make them potential cortical landmarks, and a precise alignment of them could further improve the performance of brain alignment.

However, over 300 3-hinges can be identified on a human brain (Zhang et al., 2018) and their folding morphologies are variable,

making it unfeasible to manually identify the cross-subject correspondences for all of them by the way our previous work (Li et al., 2017). Therefore, in this work, we focused on proposing an automated framework to estimate correspondence for all 3-hinges.

Specifically, we are faced with four challenges:

- 1) We attempt to match the whole 3-hinge systems. That is, by taking 3-hinges as nodes of a graph, we have to characterize its nodes and edges and match two entire graphs, but not simply searching for the alignment for each 3-hinge one by one.
- 2) The huge variability of human cortices results in different 3-hinge numbers on different subjects. Null matching will exist for a subject with more 3-hinges.
- 3) Because of the variability, cortical folding patterns (derived from structural MRI) alone may be not enough to align those cortical landmarks. Therefore, we introduce connective fiber patterns (derived from diffusion MRI, dMRI for short) to the algorithm, because connections may more directly correlate to brain function than folding patterns and thus have the potential to enhance brain alignment (Petrović et al., 2009). However, a single use of dMRI derived connective pattern, could still lead to a mismatching. For example, fibers passing anterior corpus callosum (CC) regions and posterior CC regions are both of U-shapes. Without a predefined anatomical constraint, the contralateral superior frontal gyri 3-hinge pairs have a high chance to be matched to the 3-hinge pairs on contralateral visual regions if only the fiber bundle morphology is used to measure the similarity. Therefore, A multimodal approach is likely to yield a significant improvement to the landmark alignment and even the brain alignment (Robinson et al., 2013; Zhang et al., 2013; Tardif et al., 2015).
- 4) In the pair-wise scheme, one subject will be selected as a template to which all the other subjects are matched. The selection of template subject is crucial to the results. A poor alignment could be possible when the variability is huge between the template and the target.

To tackle these challenges, we developed a two-view & group-wise graph matching method. For the first challenge, the core of our algorithm is a pair-wise graph matching method, i.e., re-weighted random walk graph matching (Cho et al., 2010). This pair-wise graph matching method is a quadratic one where both edges and nodes are matched. The quadratic graph matching problem is usually formulated as an assignment problem where an energy function is maximized. By this way, a matching between subgraphs is allowed and the second problem is solved. To tackle the third challenge, we proposed a new two-view approach with the pair-wise graph matching algorithm as the kernel to match two graphs by simultaneously considering their two different views of weight matrices. Axonal connective patterns and anatomical topological patterns represented by gyral nets (Chen et al., 2017) are used as the two views. Finally, to tackle this fourth challenge, a group-wise framework based on the two-view and pair-wise graph matching was developed, where a pseudo group-mean graph was generated in each iteration to which each graph with two views was pair-wisely matched. This pseudo group-mean graph was updated as a weighted sum of individual graphs.

The effectiveness of our method was demonstrated by the cross-subject consistency of structural connective diagrams as well as functional profiles (derived from fMRI data) on the aligned 3-hinges. In terms of the consistency, our method outperforms image- and surface-based registration methods (Jenkinson et al., 2002; Avants and Tustison, 2009; Andersson et al., 2010; Glasser et al., 2013), as well as the pair-wise or single-view graph matching methods (Cho et al., 2010). Our results provide a novel insight to the relation among cortical folding patterns, the underlying connective diagrams and brain functions, and offer new clues to inves-

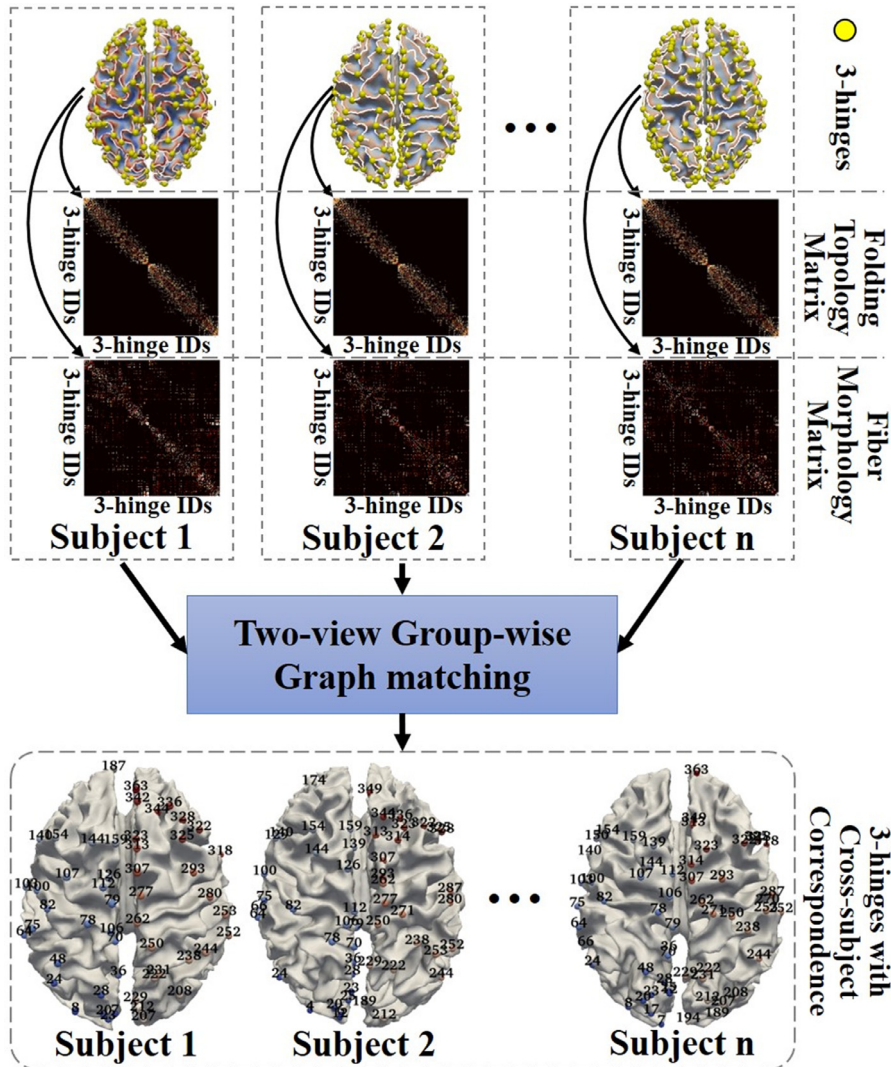


Fig. 1. Overview of the two-view and group-wise graph matching method proposed for 3-hinges' cross-subject correspondence estimation. White curves on cortical surfaces are gyral crestlines that constitute the gyral net.

tigate brain alignment on different groups of brains, such as those of diseases and other primate species.

2. Materials and Methods

2.1. MRI Dataset Description

It is worth specifying the usage of multiple datasets in this work. Cortices of macaque brains have much fewer inter-individual variabilities and a stable gyral net system as well as a stable 3-hinge system. The cross-subject correspondence of 3-hinges can be manually identified and used as the ground truth. Therefore, they provide a platform to investigate that if the dMRI derived structural connective patterns and structure MRI derived cortical folding patterns within the 3-hinge system are consistent across subjects. They can also be used to test the effectiveness of our algorithms. Our goal is to estimate 3-hinges' correspondences on human brains, which have much larger inter-individual variabilities than macaque brains. However, there is no ground truth for the correspondence on human brains. Therefore, functional MRI was used to demonstrate that the estimated structural correspondences also possess functional correspondences.

2.1.1. Macaque MRI Dataset

Macaque subjects were members of a colony at Yerkes National Primate Research Center, and MRI scans were approved by institutional animal care and use committee of Emory University. The MRI scans were performed on a Siemens 3T Trio scanner with a standard knee coil. Foam cushions, elastic straps and a designed holding device were used to minimize head motion. The imaging parameters for T1-weighted MRI are: TR=2500 ms, TE=3.49 ms, flip angle=8 deg, image matrix=256 × 256 × 192 and resolution=0.5 × 0.5 × 0.5 mm³, with 3 averages. In this study, MRI data from 18 subjects were used.

The imaging parameters for dMRI are as follows: diffusion-weighting gradients applied in 60 directions, TR/TE of 6970/104 ms, FOV of 141 × 141 mm², matrix size of 128 × 128, resolution of 1.1 × 1.1 × 1.1 mm³, 41 slices with no gap, covering the whole brain. Five images without diffusion weighting ($b=0$ s/mm²) were also acquired with matching imaging parameters.

2.1.2. Human MRI Dataset

Sixty-four subjects in the Q1 release of WU-Minn Human Connectome Project (HCP) consortium were used in this work. Important imaging parameters for T1-weighted MRI are: TR=2400 ms, TE=2.14 ms, flip angle=8 deg, image matrix=260 × 311 × 260 and

resolution=0.7 × 0.7 × 0.7 mm³. The imaging parameters for dMRI are: TR=5520 ms, TE=89.5 ms, flip angle=78 deg, FOV=210 × 180 mm², matrix=168 × 144, resolution=1.25 × 1.25 × 1.25 mm³, echo spacing=0.78 ms. Particularly, a full dMRI session includes 6 runs, representing 3 different gradient tables. Each gradient table includes approximately 90 diffusion weighting directions plus 6 $b=0$ s/mm² acquisitions interspersed throughout each run. It consists of 3 shells of $b=1000$, 2000, and 3000 s/mm² interspersed with an approximately equal number of acquisitions on each shell. For fMRI data, HCP datasets provide a resting state paradigm and seven task paradigms, including emotion, gambling, language, motor, relational, social and working memory. The task designs are referred to (Barch et al., 2013). Important acquisition parameters are as follows: 90 × 104 matrix, FOV=208 × 180 mm², 72 slices, TR=7200 s, TE=33.1 ms, flip angle=52 deg, BW =2290 Hz/Px, 2.0 mm isotropic resolution. Time points for resting state are 1200 while they vary in different tasks, which are referred to (Barch et al., 2013; Smith et al., 2013).

2.2. Data Preprocessing

For macaque data, the white matter surface was reconstructed based on T1-weighted MRI data via Freesurfer after the skull removal and tissue segmentation (Dale et al., 1999; Fischl et al., 2002; Fischl et al., 2004). Deterministic streamline fibers were reconstructed from dMRI via DSI studio (Yeh et al., 2013) after skull removal, motion correction, eddy current correction via FSL (Andersson and Sotiroopoulos, 2016; Jenkinson et al., 2012). Deterministic fiber tracking was adopted because morphological features were derived from fiber bundles to measure their similarity in the following sections. Specifically, the model-free generalized Q-sampling imaging (GQI) method (Yeh et al., 2010) in DSI Studio was adopted to estimate the density of diffusing water at different orientations. GQI method was used because it can calculate an orientation distribution function of diffusing spins from a variety of diffusion data modalities (multi-shell dMRI for human and single-shell dMRI for macaque in this work). The deterministic streamline tracking algorithm (Yeh et al., 2013) in DSI Studio was used to reconstruct 4×10^4 fiber tracts for each subject with the default fiber tracking parameters applied (max turning angle=60°, streamline length between 30 mm and 300 mm, step length=1 mm, quantitative anisotropy threshold=0.2).

The T1-weighted MRI surface was used to identify 3-hinges and their anatomical topological patterns because it provides more precise anatomical details of cortex. The anatomical metrics were derived in the original T1-weighted MRI surface space as well, in order to get rid of the impact of the nonlinear registration (for example, the length of a gyral crest could be changed after registration). Because the T1-weighted MRI surface as well as 3-hinges and white matter fiber were not in the same space, we sequentially used the linear registration method, FLIRT (Jenkinson et al., 2002), and the nonlinear registration method, FNIRT (Andersson et al., 2010; Jenkinson et al., 2012), to warp T1-weighted MRI data to the FA map in the dMRI space. Then, the linear transformation and the nonlinear warp field were applied to the white matter surfaces via Connectome Workbench¹, accordingly, such that 3-hinges, recognized as scattered points, from T1-weighted MRI surface were warped to dMRI space as well. This step further improves the accuracy of extracting dMRI fibers and deriving connective matrix within 3-hinges (detailed in section 2.5). White matter surfaces were also derived from FA maps. These surfaces were used for visualization in most cases, especially when dMRI fibers were pre-

sented, because there are no cross-modality registration errors between these surfaces and fibers.

For human data, the preprocessing pipelines for T1-weighted MRI and dMRI were the same as the ones for macaque. As for fMRI data, HCP dataset provides a grayordinate system for each subject. A standard grayordinate system consists of a cortical surface mesh and subcortical volume parcels in the MNI standard space (Glasser, et al., 2013). Each vertex on this surface was associated with a corresponding functional MRI signal that has been preprocessed via the minimal preprocessing pipelines (Glasser, et al., 2013). Because the grayordinate surface was also reconstructed from the T1-weighted MRI, it is easy to use the aforementioned linear and non-linear registration methods to warp the grayordinate surface to the dMRI space.

2.3. Method Overview

Our goal is to estimate cross-individual correspondence for 3-hinges via simultaneously matching their folding topology and connective diagram (Fig. 1). Therefore, in section 2.4, we firstly introduce how to identify locations of 3-hinges (yellow bubbles in Fig. 1). For each subject, its 3-hinges can be taken as nodes of a graph. On this graph, we introduce in section 2.5 how to derive two types of features from two different views and how to present them as the edges of the graph (the 2nd and the 3rd rows in Fig. 1): the cortical folding topology (gyral net, white curves on the surfaces) and fiber connective diagram (fiber morphological feature). Then, we introduce in section 2.6.1 how to formulate the 3-hinges correspondence estimation problem into a graph matching one. The basics of a classic pair-wise graph matching algorithm (Cho et al., 2010) are introduced in section 2.6.2. Next, we introduce in section 2.6.3 how to match two graphs with two different weight matrices (two-view graph matching). By far, the graph matching is performed between a pair of subjects, and we finally introduce in section 2.6.4 how to perform a group-wise graph matching for the cohort.

2.4. Identification of 3-hinges

The 3-hinges were identified via a home-made automated approach (Chen et al., 2017). We provide a summary of the approach to make this manuscript self-contained. This approach consists of four major steps:

First, gyral altitudes were computed and mapped to the surfaces (Fig. 2(a-c)). The gyral altitude is the displacement of a vertex on a surface from a hypothetical “mid-surface” that exists between the gyri and sulci to its original location. This “mid-surface” is chosen so that the mean of the displacements of all surface vertices from their original locations is zero (Fischl, et al., 1999b). White ribbons between red regions and blue regions in Fig. 2(b) indicate the intersection of the hypothetical “mid-surface” and the original surface. The displacements of the vertices in the red region (gyri, above the “mid-surface”) are positive and the ones in blue regions (sulci, below the “mid-surface”) are negative, and they sum to 0. The displacements (or gyral altitudes) were mapped to all vertices of the surface in Fig. 2(c).

Second, the watershed algorithm (Bertrand, 2005) was applied to the altitude map in Fig. 2(c) to separate gyri from sulci. In fact, the white ribbons in Fig. 2(b) can be taken as the water level of 0. On the gyral regions, a tree marching algorithm was applied to the altitude map. The roots of the trees are located at the centers of gyri which usually have the local gyral altitude maxima. Then, starting from the roots, vertices were progressively connected and the tree structure expansion followed the descending gradient of the gyral altitudes till the border between gyri and sulci was reached.

¹ <https://www.humanconnectome.org/software/connectome-workbench>

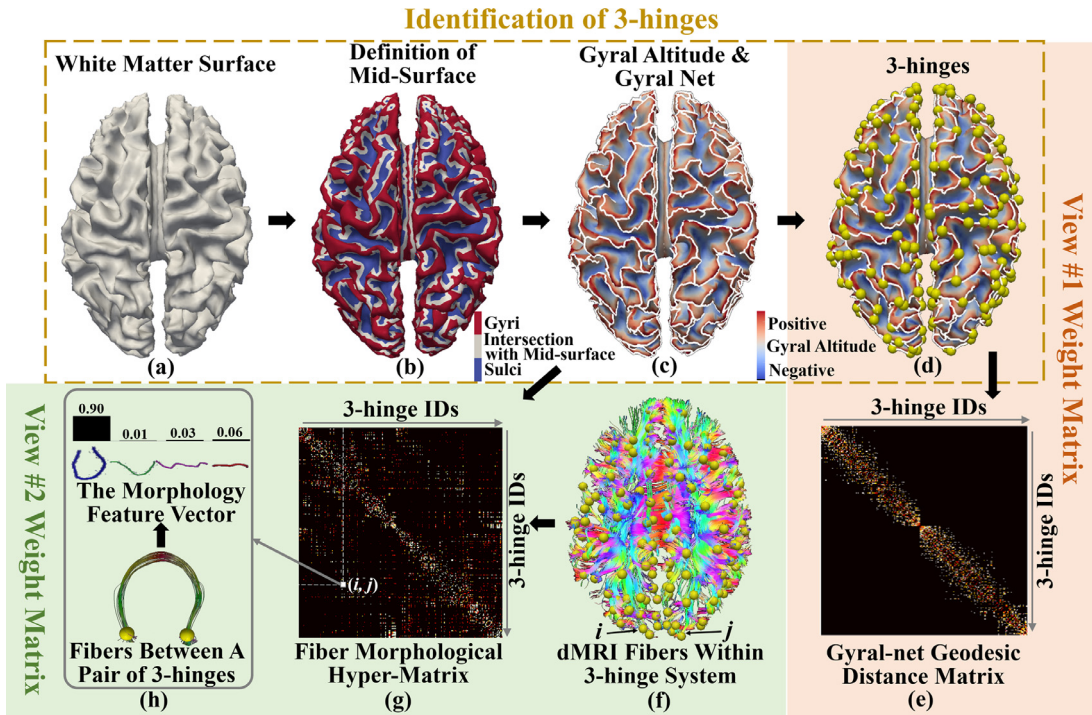


Fig. 2. Schematics of 3-hinge identification (yellow frame): (a) A white matter cortical surface. (b) Determination of the hypothetical ‘mid-surface’. White ribbons indicate the intersection of the ‘mid-surface’ and the original surface. Displacements of vertices red regions have positive values while those in the blue regions have negative values. All displacements sum to 0. (c) The displacements were defined as the gyral altitudes. The surface is color-coded by gyral altitudes. Positive/negative altitude values are represented by red/blue colors. White curves are the gyral net. (d) Yellow bubbles indicate the locations of 3-hinges, where three branches on the gyral net meet each other. By taking 3-hinges as nodes of a graph, we derived weight matrices of the two views (pink panel and green panel): (e) View #1: Geodesic distance matrix, the edges of which are the branch length on the gyral net between a pair of 3-hinges. (f)-(h) View #2: Fiber morphological hyper-matrix. To obtain this matrix, dMRI deterministic fibers were extracted from the 3-hinge system (illustrated in (f)). The fiber bundle between a pair of 3-hinges (i, j) was extracted and a morphology feature vector was developed from this fiber bundle (illustrated in (h)). In the fiber morphological hyper-matrix (g), the edge (i, j) is the feature vector in (h).

Third, the short branches were trimmed from the tree structure when their length was below a threshold. By this way, the main trunks of the tree structures were preserved and defined as a “gyral net” (white curves in Fig. 2(c)).

Finally, on this gyral net, the conjunctions of three branches were defined as 3-hinges (yellow bubbles in Fig. 2(d)).

It is noted that folding patterns of macaque brains have much higher cross-subject consistency than those of human brains, we used a semi-automatic approach to identify the gyral net and 64 3-hinges on each macaque hemisphere. Specifically, we firstly applied the gyral-net and 3-hinges detection algorithm on the macaque template surface of the “F99” atlas (Van Essen, 2011). Some obvious noisy hinges as well as the gyral crests were manually removed. Importantly, the connectedness between the finalized hinges on this template was recorded. Second, because the cortical folding patterns, especially the gyral topology, are consistent across macaque brains, we used surface registration in FreeSurfer to warp the finalized 64 hinges as well as the gyral net to each individual surface. Finally, Locations of a very few 3-hinges on individual surfaces were manually improved to ensure that they were in the centers of gyral crossings. The gyral net crest lines that are attached to these manually improved 3-hinges also need to update. To this end, we adopted the fast-marching algorithm to track the gyral crest line between the moved hinges and the other hinges according to the recorded connectedness. By giving a higher marching speed to the vertices with higher gyral altitude, we restricted the geodesic paths within the gyral crests. By this way, we obtained the 3-hinges and the gyral net on a macaque surface and the cross-subject correspondence was guaranteed.

2.5. Weight Matrices of 3-hinges System from Two-views

By taking 3-hinges as the nodes of a graph, we defined two different types of edge attributes and derived two corresponding weight matrices.

- 1) gyral net geodesic length matrix (Fig. 2(e)): the length of a branch that directly connects a pair of 3-hinges on the gyral net was used as the weight. This matrix encodes the topological pattern of the gyral net. To remove the effect of brain size, the length of a branch was normalized by dividing it by the square root of the total cortical area of a subject.
- 2) fiber bundle morphological feature matrix (Fig. 2(f-h)): this is a hyper-matrix, where the element between a pair of 3-hinges (i, j) is a feature vector (Fig. 2(h)). To obtain the feature vector, fibers within the 3-hinge system were firstly extracted (Fig. 2(f)). In order to ensure that the feature vector is comparable across subjects, all such fibers of the entire cohort were classified to 4 basic shapes (Zhang et al., 2014). The cluster centers are shown in Fig. 2(h). Based on this classification result, each fiber was associated with a class label. Then, the fibers between a pair of 3-hinges (i, j) were extracted (lower part of Fig. 2(h)) and the distribution histogram of 4 shape classes within this bundle was used as the morphological feature vector (the bins in Fig. 2(h)).

By far, each subject has a 3-hinge graph which is associated with two different weight matrices. The two different matrices can be taken as two views for the same 3-hinge graph. One encodes the anatomical topology and the other encodes the axonal connective diagram. It is noted that subjects have different numbers of

3-hinges (267~369, 275.25 ± 34.64), such that the 3-hinge graphs from different subjects are of different sizes.

2.6. Two-view & Group-wise Graph Matching

2.6.1. Problem Formulation

In our application, 3-hinges from a subject were defined as the nodes of a graph. The features of fiber bundles or the gyral net branches were defined as edge attributes. Matching two such 3-hinge graphs from two subjects can thus be converted to a quadratic graph matching problem. Let $\mathbf{G}^P = (\mathbf{V}^P, \mathbf{E}^P, \mathbf{A}^P)$ and $\mathbf{G}^Q = (\mathbf{V}^Q, \mathbf{E}^Q, \mathbf{A}^Q)$ to denote two graphs from subject #P and #Q. \mathbf{V} denotes a set of nodes. \mathbf{E} denotes the edges. \mathbf{A} denotes the weight matrix, where a_{ij}^P denotes the edge attribute for $e_{ij}^P \in \mathbf{E}^P$. In our problem, nodal feature a_i^P was not used. To quadratically match two graphs, an affinity matrix \mathbf{W} is defined where $w_{ia;jb}$ describes the consistency of attributes between the node pairs of candidate correspondences (v_i^P, v_a^Q) and (v_j^P, v_b^Q) . \mathbf{W} is usually obtained from \mathbf{A}^P and \mathbf{A}^Q . A diagonal element $w_{ia;ia}$ represents the nodal similarity between (v_i^P, v_a^Q) while the off-line element $w_{ia;jb}$ measures the similarity between the pair of edges $e_{ij}^P \in \mathbf{E}^P$ and $e_{ab}^Q \in \mathbf{E}^Q$ in terms of their edge attributes a_{ij}^P and a_{ab}^Q . By using an assignment matrix $\mathbf{X} \in \{0, 1\}^{n^P \times n^Q}$, where $x_{ia} = 1$ indicates that v_i^P corresponds to v_a^Q , the graph matching problem is usually formulated as an integer quadratic program that searches for the vector \mathbf{x}^* (\mathbf{x} is a column-wise vector converted from \mathbf{X}) that maximizes the following quadratic score function:

$$\begin{aligned} \mathbf{x}^* = \arg \max_{\mathbf{x}} (\mathbf{x}^T \mathbf{W} \mathbf{x}), \text{ s.t. } \mathbf{x} \in \{0, 1\}^{n^P n^Q}, \forall i \sum_{a=1}^{n^Q} x_{ia} \leq 1, \\ \forall a \sum_{i=1}^{n^P} x_{ia} \leq 1 \end{aligned} \quad (1)$$

where the two-way constraints $\forall i \sum_{a=1}^{n^Q} x_{ia} \leq 1$, $\forall a \sum_{i=1}^{n^P} x_{ia} \leq 1$ enforce the one-to-one correspondence between \mathbf{V}^P and \mathbf{V}^Q .

2.6.2. Basics of Pair-wise Reweighted Random Walk Algorithm

Finding a vector \mathbf{x}^* that maximizes function in Eq. (1) is NP-complete. Reweighted random walk algorithm is one of the methods that find suboptimal solutions.

The basic algorithm of the reweighted random walk graph matching is as follows:

Algorithm 1. Reweighted random walk graph matching

- 1: Given the affinity matrix \mathbf{W} , parameter α and β , initialize \mathbf{x} as uniform
 - 2: Set $\mathbf{W}_{(ia,jb)} = 0$ for all conflicting match pairs
 - 3: Update matrix $\mathbf{W} = \mathbf{W}/d_{max}$, where $d_{max} = \max_{ia} \sum_{jb} \mathbf{W}_{(ia,jb)}$
 - 4: Begin A: (Do A until \mathbf{x} converges)
 - 5: $\hat{\mathbf{x}}^T = \mathbf{x}^T \mathbf{W}$
 - 6: $\hat{\mathbf{x}} = \exp(\beta \hat{\mathbf{x}} / \max \hat{\mathbf{x}})$
 - 7: Begin B: (Do B until $\hat{\mathbf{x}}$ converges)
 - 8: Normalize across all rows: $\hat{\mathbf{x}}_{ai} = \hat{\mathbf{x}}_{ai} / \sum_{i=1}^I \hat{\mathbf{x}}_{ai}$
 - 9: Normalize across all columns: $\hat{\mathbf{x}}_{ai} = \hat{\mathbf{x}}_{ai} / \sum_{a=1}^A \hat{\mathbf{x}}_{ai}$
 - 10: End B
 - 11: $\hat{\mathbf{x}} = \hat{\mathbf{x}} / \sum \hat{\mathbf{x}}_{ai}$
 - 12: $\mathbf{x}^T = \alpha \hat{\mathbf{x}}^T + (1 - \alpha) \hat{\mathbf{x}}^T$
 - 13: $\mathbf{x} = \mathbf{x} / \sum x_{ai}$
 - 14: End A
 - 15: \mathbf{x} is discretized by the Hungarian algorithm (Munkres, 1957).
-

More interpretations of some steps are as follows:

- 1 The step in line #2 is to prevent the predefined unexpected matches. In our application, we simply do not allow the matching between two hemispheres.
- 2 In line #3, the affinity matrix \mathbf{W} is updated by dividing by the maximum degree. Usually, the affinity matrix in random walk is converted to the row stochastic matrix by $\mathbf{W} = \mathbf{D}^{-1} \mathbf{W}$. \mathbf{D} is a diagonal matrix and the diagonal elements are the row degrees. However, in our application, two graphs often have different sizes causing many false candidate correspondences. $\mathbf{D}^{-1} \mathbf{W}$ will scale up the affinities of those false correspondences in \mathbf{W} . Using the maximum degree instead can prevent this problem by preserving the relative affinity relation while converting the affinity matrix to a stochastic one. More explanations are referred to Cho et al., 2010.
- 3 In line #5, \mathbf{x} is updated via the affinity-preserving random walking by edges. This step can also be interpreted from the perspective of solving an assignment function maximization problem (Gold and Rangarajan, 1996). We recall that the graph matching problem is equivalent to the maximization of $\mathbf{x}^T \mathbf{W} \mathbf{x}$ in Eq. (1). Given an initial indicator vector $\mathbf{x}^{(0)}$, the objective function can be expanded via a Taylor series approximation:

$$\begin{aligned} E(\mathbf{x}) = \mathbf{x}^T \mathbf{W} \mathbf{x} \approx \mathbf{x}^{(0)T} \mathbf{W} \mathbf{x}^{(0)} + \frac{\partial E}{\partial \mathbf{x}} \Big|_{\mathbf{x}=\mathbf{x}^{(0)}} (\mathbf{x} - \mathbf{x}^{(0)}) \\ = \mathbf{x}^{(0)T} \mathbf{W} \mathbf{x}^{(0)} + 2 \mathbf{x}^{(0)T} \mathbf{W} (\mathbf{x} - \mathbf{x}^{(0)}) \end{aligned} \quad (2)$$

where the term $2 \mathbf{x}^{(0)T} \mathbf{W} \mathbf{x}$ coincides with the one $\hat{\mathbf{x}}^T = \mathbf{x}^T \mathbf{W}$ in line #5.

It is noted that this alternative interpretation in Eq. (2) will be used to develop the two-view graph matching method in section 2.6.3.

- 1 Introduction of β in line #6 and normalization in line #11 are to convert the discrete assignment problem ($\mathbf{x} \in \{0, 1\}^{n^P \times n^Q}$ in Eq. (1)) to a continuous one, which is also known as the softmax (Gold and Rangarajan, 1996). With a large β , $\hat{\mathbf{x}}_i$ will be close to 1 if $\hat{\mathbf{x}}_i$ is the maximum, while the others approach 0.
- 2 The normalization steps in line 8 & 9 are used to satisfy the two-way constraint $\forall i \sum_{a=1}^{n^Q} x_{ia} \leq 1$, $\forall a \sum_{i=1}^{n^P} x_{ia} \leq 1$ in Eq. (1), such that a node in \mathbf{G}^P corresponds to only one node in \mathbf{G}^Q and vice versa. This constraint is also used as a reweighted jump which is integrated to \mathbf{x} in line 12.

2.6.3. Pair-wise Graph Matching Algorithm with Two-views

In this section, we introduce how to extend the basic algorithm in the previous section to a two-view graph matching method. We used $\mathbf{G} = (\mathbf{V}, \{\mathbf{EV}^1, \mathbf{AV}^1\}, \{\mathbf{EV}^2, \mathbf{AV}^2\})$ to denote a graph with two views. In our application, \mathbf{EV}^1 is the set of fiber bundles that connect pairs of 3-hinges. \mathbf{AV}^1 is a hyper weight matrix, the element of which is the morphological vector of the fiber bundle. \mathbf{EV}^2 is the set of branches in gyral net that connect direct pairs of 3-hinges. Element of \mathbf{AV}^2 is the geodesic length of a branch. The two sets of edges and edge attributes share the same set of nodes \mathbf{V} .

For the two views, we have two affinity matrices \mathbf{W}_1 and \mathbf{W}_2 and two corresponding assignment vectors \mathbf{x} and \mathbf{y} . $\mathbf{w}_{ia;jb}$ is defined as $\exp(-a_{ij}^P - a_{ab}^Q / \sigma^2)$ where $a_{ij}^P - a_{ab}^Q$ is the l_2 norm that measures the similarity between edge $e_{ij}^P \in \mathbf{E}^P$ and $e_{ab}^Q \in \mathbf{E}^Q$. For \mathbf{W}_1 , $\mathbf{w}_{ia;jb}$ is the similarity between fiber bundle feature vector. For \mathbf{W}_2 , $\mathbf{w}_{ia;jb}$ is the similarity between geodesic length on gyral net.

According to Eq. (1), maximizing $\mathbf{x}^T \mathbf{W}_1 \mathbf{x}$ and $\mathbf{y}^T \mathbf{W}_2 \mathbf{y}$ separately will yield the desired \mathbf{x} and \mathbf{y} , respectively. However, we expect that the yielded two assignment vectors agree with each other. We thus added a couple of terms to Eq. (1). The first term is $\mathbf{x}^T \mathbf{y}$, which measures the disagreement between the assignments

of two views. A greater agreement between \mathbf{x} and \mathbf{y} gives a larger value. Also, the assignment vector from one view is expected to impose its impact on the affinity matrix of the other view. To this end, $0.5\mathbf{x}^T\mathbf{W}_1\mathbf{y} + 0.5\mathbf{y}^T\mathbf{W}_1\mathbf{x} + 0.5\mathbf{y}^T\mathbf{W}_2\mathbf{x} + 0.5\mathbf{x}^T\mathbf{W}_2\mathbf{y}$ was introduced. The factor 0.5 was used to scale the weights of the four terms to match the original term $\mathbf{x}^T\mathbf{W}_1\mathbf{x} + \mathbf{y}^T\mathbf{W}_2\mathbf{y}$. Because \mathbf{W}_1 and \mathbf{W}_2 in our application are symmetric, this term can be replaced by $\mathbf{x}^T\mathbf{W}_1\mathbf{y} + \mathbf{y}^T\mathbf{W}_2\mathbf{x}$.

The final form of the energy function for two-views is as follows:

$$\begin{aligned} E(\mathbf{x}, \mathbf{y}) &= \mathbf{x}^T\mathbf{W}_1\mathbf{x} + \mathbf{y}^T\mathbf{W}_2\mathbf{y} + \mathbf{x}^T\mathbf{W}_1\mathbf{y} + \mathbf{y}^T\mathbf{W}_2\mathbf{x} + \beta\mathbf{x}^T\mathbf{y}, \text{ s.t. } \mathbf{x}, \\ \mathbf{y} \in \{0, 1\}^{n^P n^Q}, \quad \forall i \sum_{a=1}^{n^Q} \mathbf{x}_{ia} &\leq 1, \quad \forall a \sum_{i=1}^{n^P} \mathbf{x}_{ia} \leq 1, \quad \forall i \sum_{a=1}^{n^Q} \mathbf{y}_{ia} \leq 1, \\ \forall a \sum_{i=1}^{n^P} \mathbf{y}_{ia} &\leq 1 \end{aligned}$$

The Taylor series approximation is as follows:

$$E(\mathbf{x}, \mathbf{y}) \approx E(\mathbf{x}^{(0)}, \mathbf{y}^{(0)}) + \frac{\partial E}{\partial \mathbf{x}}|_{\mathbf{x}^{(0)}, \mathbf{y}^{(0)}} (\mathbf{x} - \mathbf{x}^{(0)}) + \frac{\partial E}{\partial \mathbf{y}}|_{\mathbf{x}^{(0)}, \mathbf{y}^{(0)}} (\mathbf{y} - \mathbf{y}^{(0)}) = \mathbf{ax} + \mathbf{by} + \mathbf{c}$$

where

$$\begin{cases} a = 2\mathbf{x}^{(0)T}\mathbf{W}_1 + \mathbf{y}^{(0)T}(\mathbf{W}_1 + \mathbf{W}_2 + \beta\mathbf{I}) \\ b = 2\mathbf{y}^{(0)T}\mathbf{W}_2 + \mathbf{x}^{(0)T}(\mathbf{W}_1 + \mathbf{W}_2 + \beta\mathbf{I}) \\ c = -\mathbf{x}^{(0)T}\mathbf{W}_1\mathbf{x}^{(0)} - \mathbf{y}^{(0)T}\mathbf{W}_2\mathbf{y}^{(0)} - \mathbf{y}^{(0)T}\mathbf{W}_1\mathbf{x}^{(0)} - \mathbf{x}^{(0)T}\mathbf{W}_2\mathbf{y}^{(0)} \\ \quad - \beta\mathbf{x}^{(0)T}\mathbf{y}^{(0)} \end{cases} \quad (4)$$

and \mathbf{I} is an identity matrix.

The two assignment vectors \mathbf{x} and \mathbf{y} can be alternately updated in each iteration. The two-view graph matching algorithm is as follows:

Algorithm 2. Reweighted random walk graph matching with 2 views

- 1: Given the affinity matrices \mathbf{W}_1 and \mathbf{W}_2 , parameter α and β ; initialize \mathbf{x} and \mathbf{y} as uniform
 - 2: Set $\mathbf{W}_k(ia, jb) = 0$, $k \in \{1, 2\}$ for all conflicting match pairs
 - 3: Updated matrix $\mathbf{W}_k = \mathbf{W}_k/d_{k \max}$, where $d_{k \max} = \max_{ia} \sum_{jb} \mathbf{W}_k(ia, jb)$, $k \in \{1, 2\}$
 - 4: Begin A: (Do A until \mathbf{x} and \mathbf{y} converges)
 - 5: $\hat{\mathbf{x}}^T = 2\mathbf{x}^T\mathbf{W}_1 + \mathbf{y}^T(\mathbf{W}_1 + \mathbf{W}_2 + \beta\mathbf{I})$, $\hat{\mathbf{y}}^T = 2\mathbf{y}^T\mathbf{W}_2 + \mathbf{x}^T(\mathbf{W}_1 + \mathbf{W}_2 + \beta\mathbf{I})$
 - 6: $\hat{\mathbf{x}} = \exp(\beta\hat{\mathbf{x}}/\max\hat{\mathbf{x}})$
 - 7: Begin B: (Do B until $\hat{\mathbf{x}}$ converges)
 - 8: Normalize across all rows: $\hat{\mathbf{x}}_{ai} = \hat{\mathbf{x}}_{ai}/\sum_{i=1}^A \hat{\mathbf{x}}_{ai}$
 - 9: Normalize across all columns: $\hat{\mathbf{x}}_{ai} = \hat{\mathbf{x}}_{ai}/\sum_{a=1}^A \hat{\mathbf{x}}_{ai}$
 - 10: End B
 - 11: $\hat{\mathbf{x}} = \hat{\mathbf{x}}/\sum \hat{\mathbf{x}}_{ai}$
 - 12: $\mathbf{x}^T = \alpha\hat{\mathbf{x}}^T + (1 - \alpha)\mathbf{x}^T$
 - 13: $\mathbf{x} = \mathbf{x}/\sum \mathbf{x}_{ai}$
 - 14: $\hat{\mathbf{y}} = \exp(\beta\hat{\mathbf{y}}/\max\hat{\mathbf{y}})$
 - 15: Begin C: (Do B until $\hat{\mathbf{y}}$ converges)
 - 16: Normalize across all rows: $\hat{\mathbf{y}}_{ai} = \hat{\mathbf{y}}_{ai}/\sum_{i=1}^A \hat{\mathbf{y}}_{ai}$
 - 17: Normalize across all columns: $\hat{\mathbf{y}}_{ai} = \hat{\mathbf{y}}_{ai}/\sum_{a=1}^A \hat{\mathbf{y}}_{ai}$
 - 18: End C
 - 19: $\hat{\mathbf{y}} = \hat{\mathbf{y}}/\sum \hat{\mathbf{y}}_{ai}$
 - 20: $\mathbf{y}^T = \alpha\hat{\mathbf{y}}^T + (1 - \alpha)\mathbf{y}^T$
 - 21: $\mathbf{y} = \mathbf{y}/\sum \mathbf{y}_{ai}$
 - 22: End A
 - 23: \mathbf{x} is discretized by the Hungarian algorithm (Munkres, 1957). It is noted that $\mathbf{x} = \mathbf{y}$.
-

2.6.4. Group-wise Graph Matching Algorithm

In this section, we introduce how to extend the pair-wise matching to a group-wise scheme. Suppose we have n subjects, each of which has a two-view graph $\mathbf{G}_n = (\mathbf{V}_n, \{\mathbf{E}_n^{V_1}, \mathbf{A}_n^{V_1}\}, \{\mathbf{E}_n^{V_2}, \mathbf{A}_n^{V_2}\})$. In each iteration, a mean graph

$\mathbf{M} = (\mathbf{V}_M, \{\mathbf{E}_M^{V_1}, \mathbf{A}_M^{V_1}\}, \{\mathbf{E}_M^{V_2}, \mathbf{A}_M^{V_2}\})$ was yielded where the weight matrices $\mathbf{A}_M^{V_1}$ and $\mathbf{A}_M^{V_2}$ are the weighted sum of all weight matrices $\mathbf{A}_n^{V_1}$ and $\mathbf{A}_n^{V_2}$, respectively. The group-mean graph \mathbf{M} were used as the “template” in the next iteration, to which individual \mathbf{G}_n was matched, respectively, via the two-view pair-wise matching in **Algorithm 2**.

Node number k for \mathbf{M} was determined to be the same as the subject that has the largest number of nodes. k for \mathbf{M} remains the same across all iterations. To yield the group mean graph, null nodes were added to individual graphs \mathbf{G}_n , such that the graphs with fewer nodes also have k nodes. Accordingly, null edges were added to $\{\mathbf{E}_n^{V_1}, \mathbf{E}_n^{V_2}\}$ and empty rows and columns (values of 0s) were added to the weight matrices $\{\mathbf{A}_n^{V_1}, \mathbf{A}_n^{V_2}\}$. Therefore, when \mathbf{M} was updated in the next iteration, those empty edges were not considered.

In the t^{th} iteration, **Algorithm 2** was applied to the pair of the group-mean weight matrices $\{\mathbf{A}_M^{V_1}|_{t-1}, \mathbf{A}_M^{V_2}|_{t-1}\}$ from the $(t-1)^{th}$ iteration and the n^{th} subject $\{\mathbf{A}_n^{V_1}|_t, \mathbf{A}_n^{V_2}|_t\}$. $\{\mathbf{A}_n^{V_1}|_t, \mathbf{A}_n^{V_2}|_t\}$ were updated as $\{\hat{\mathbf{A}}_n^{V_1}|_t, \hat{\mathbf{A}}_n^{V_2}|_t\}$ by the obtained assignment vector \mathbf{x}_n^t (It is noted that the assignment vector for two views \mathbf{x}_n^t and \mathbf{y}_n^t are equal). This step is indicated by the black, red and green arrows in Fig. 3. Black arrows indicate the pair-wise graph matching within a view (the first two terms in Eq. (3)) and red and green arrows indicate the matching intra-views (the last three terms in Eq. (3)). Then, the group means $\{\mathbf{A}_M^{V_1}|_t, \mathbf{A}_M^{V_2}|_t\}$ were updated as the weighted sum of $\{\hat{\mathbf{A}}_n^{V_1}|_t, \hat{\mathbf{A}}_n^{V_2}|_t\}$ s. The weights were computed for each view, separately. The similarity between $\hat{\mathbf{A}}_n|_t$ and $\mathbf{A}_M|_{t-1}$ was used as the weight $w_n|_t$, which was defined as the energy $w_n|_t = \mathbf{x}_n^T \mathbf{W}_{\hat{\mathbf{A}}_n|_t, \mathbf{A}_M|_{t-1}} \mathbf{x}_n^t$ after matching. The weight was normalized as $w_n|_t = w_n|_t / \sum w_n|_t$. In circumstances where \mathbf{A}_n vary hugely across subjects (especially in the starting iterations), similar weights could possibly yield blurred \mathbf{A}_M that could possibly mislead the matching between \mathbf{A}_n s and \mathbf{A}_M . This misleading could further prevent yielding an effective group mean \mathbf{A}_M in the next iteration. Therefore, we used $w_n|_t = \exp(\varepsilon w_n|_t) / \sum \exp(\varepsilon w_n|_t)$ to further update $w_n|_t$ s, making a larger $w_n|_t$ approaches 1, and approaches 0, otherwise. The initial $\mathbf{A}_M|_0$ is the sum of all the original $\mathbf{A}_n|_0$ s with equal weights. The algorithm stops when there is no more difference between two successive $\{\mathbf{A}_n^{V_1}, \mathbf{A}_n^{V_2}\}$ s.

This group-wise graph matching algorithm is summarized in Algorithm 3 as follows:

Algorithm 3. Group-wise graph matching with two views

- 1: Given two groups of weight matrices $\{\mathbf{A}_1^{V_1}, \mathbf{A}_2^{V_1}, \dots, \mathbf{A}_n^{V_1}\}$ and $\{\mathbf{A}_1^{V_2}, \mathbf{A}_2^{V_2}, \dots, \mathbf{A}_n^{V_2}\}$ of two views, γ , δ and ε .
 - 2: Normalize the size: $\mathbf{A}_n^V = \begin{bmatrix} \mathbf{A}_n^V & \mathbf{0}_1 \\ \mathbf{0}_1^T & \mathbf{0}_2 \end{bmatrix}$, where the size of the updated \mathbf{A}_n^V is $k = \max(\{\|\mathbf{A}_n^V\|\})$, where $v \in \{v_1, v_2\}$.
 - 3: Initialize weight vectors $\mathbf{w}_n^{V_1}|_0$ and $\mathbf{w}_n^{V_2}|_0$ as uniform
 - 4: Initialize group means $\mathbf{A}_M^V|_0 = \sum \mathbf{A}_n^V * \mathbf{w}_n^V|_0$, where $v \in \{v_1, v_2\}$
 - 5: Initialize loop control parameters $t=1$, $r^{V_1}=0$, $r^{V_2}=0$
 - 6: Begin A: (Do A until $r^{V_1} \leq \gamma$ and $r^{V_2} \leq \gamma$, or $t \geq \delta$)
 - 7: Performing pair-wise two-view graph matching between $\{\mathbf{A}_n^{V_1}|_t, \mathbf{A}_n^{V_2}|_t\}$ and $\{\mathbf{A}_M^V|_{t-1}, \mathbf{A}_M^V|_{t-1}\}$ by feeding the affinity matrix $\{\mathbf{W}_n^{V_1}|_t, \mathbf{W}_n^{V_2}|_t\}$ to Algorithm 2 to yield the assignment vector \mathbf{x}_n^t . Update $\{\mathbf{A}_n^{V_1}|_t, \mathbf{A}_n^{V_2}|_t\}$ to $\{\hat{\mathbf{A}}_n^{V_1}|_t, \hat{\mathbf{A}}_n^{V_2}|_t\}$ by \mathbf{x}_n^t .
 - 8: Compute weights: $\mathbf{w}_n^{V_1}|_t = \mathbf{x}_n^T \mathbf{W}_n^{V_1}|_t \mathbf{x}_n^t$, and update weights: $\mathbf{w}_n^{V_1}|_t = \mathbf{w}_n^{V_1}|_t / \sum \mathbf{w}_n^{V_1}|_t$, $\mathbf{w}_n^{V_1}|_t = \exp(\varepsilon \mathbf{w}_n^{V_1}|_t) / \sum \exp(\varepsilon \mathbf{w}_n^{V_1}|_t)$ and $\mathbf{w}_n^{V_2}|_t = \mathbf{w}_n^{V_2}|_t / \sum \mathbf{w}_n^{V_2}|_t$, where $v \in \{v_1, v_2\}$
 - 9: Update group mean $\mathbf{A}_M^V|_t = \sum \hat{\mathbf{A}}_n^V |_t * \mathbf{w}_n^V|_t$ and individual weight matrices $\mathbf{A}_n^V|_{t+1} = \hat{\mathbf{A}}_n^V|_t$, where $v \in \{v_1, v_2\}$
 - 10: $r^{V_1} = \sum \mathbf{A}_n^V|_t - \mathbf{A}_M^V|_{t-1}|$, where $v \in \{v_1, v_2\}$, $t=t+1$
 - 11: End A
 - 12: End C
 - 13: Return the latest $\{\mathbf{x}_n^t\}$, which record the final cross-subject correspondences.
-

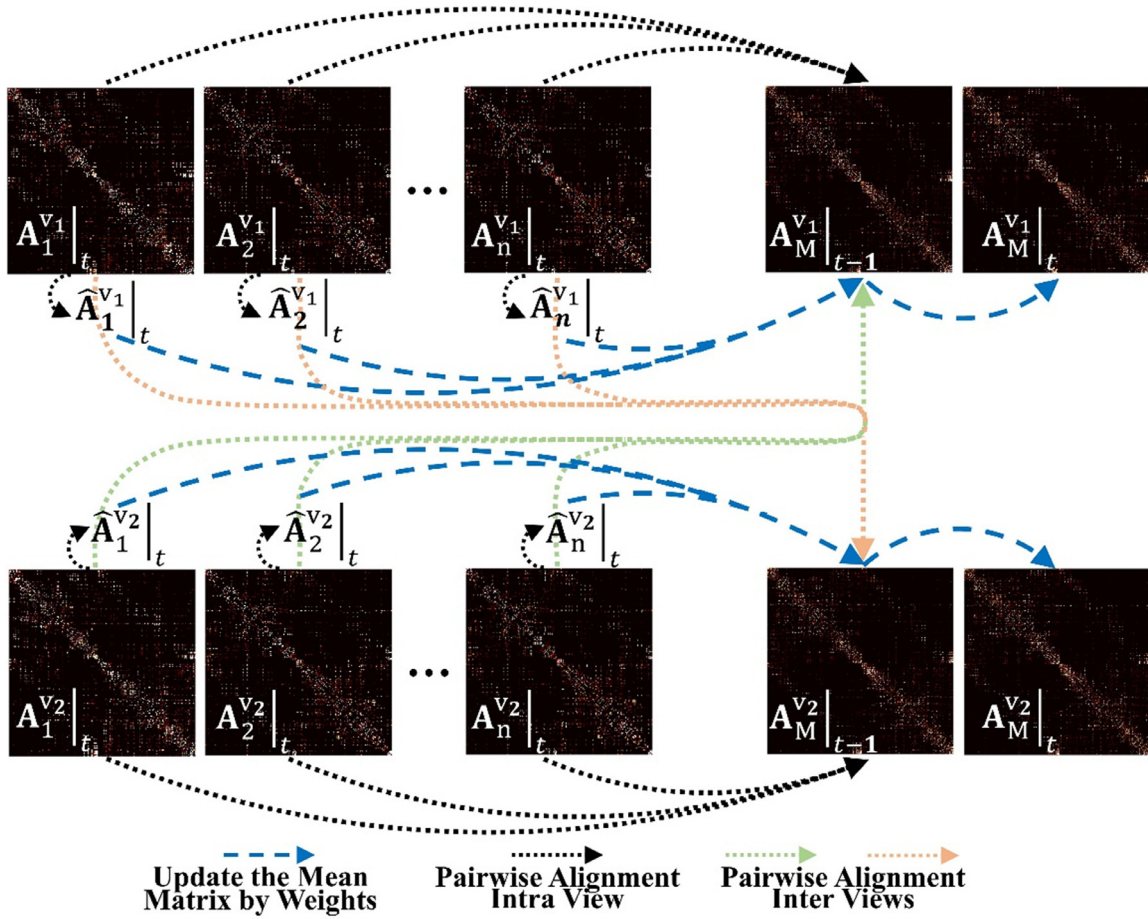


Fig. 3. A schematic diagram of the group-wise and two-view graph matching framework. In the t^{th} iteration, the weight matrices of two views of each subject $\{A_n^{v_1}|_t, A_n^{v_2}|_t\}$ was matched to the group mean ones $\{A_M^{v_1}|_{t-1}, A_M^{v_2}|_t\}$ of the $(t-1)^{th}$ iteration. This matching is conducted in a pair-wise manner via the two-view matching algorithm (Algorithm 2). Black arrows indicate the pair-wise graph matching within a view (the first two terms in Eq. (3)). Red and green arrows indicate the matching intra-views (the last three terms in Eq. (3)). Then, within each view, the similarity between the updated individual graph and the group mean was measured and the similarity was used as weight. Finally, the group means $\{A_M^{v_1}|_t, A_M^{v_2}|_t\}$ were separately updated as the weighted sum of individual matrices (blue arrows).

2.7. Evaluations

We evaluated the estimated 3-hinge correspondences by means of the following methods. It is noted that null 3-hinges have been added to the subjects which have fewer 3-hinges than the maximum number k before the group-wise matching was performed. Therefore, there are non-assignments corresponding to null 3-hinges in vectors $\{\mathbf{x}_n^t\}$.

1) Group-wise 3-hinge indices assignment consistency

After the graph matching, each 3-hinge has cross-subject corresponding index and each subject has an index vector of all 3-hinges. In our framework, only one-to-one matching was allowed, and there is no repeating index within each 3-hinge index vector. Null labels were assigned to those null 3-hinges to make all label vectors having the same size. We expect that the 3-hinge index vectors are similar across subjects. We thus used intraclass correlation coefficient (ICC) to measure the group-wise consistency of the 3-hinge index vectors from all subjects. A higher r value in ICC indicates a higher cross-subject consistency of the index vectors.

2) Structural metrics

To compute the similarity between two matrices, we adopted the Pearson correlation coefficient. Let \mathbf{X} and \mathbf{Y} denote two matrices of the same size. Because the matrices are symmetric, their upper triangular parts were converted to vectors \mathbf{x} and \mathbf{y} . The con-

ventional Pearson's correlation coefficient (PCC) between two vectors was computed as follows:

$$r = \frac{\sum_{i=1}^n (x_i - \bar{x})(y_i - \bar{y})}{\sqrt{\sum_{i=1}^n (x_i - \bar{x})^2} \sqrt{\sum_{i=1}^n (y_i - \bar{y})^2}} \quad (5)$$

where x_i and y_i are the sample in \mathbf{x} and \mathbf{y} . \bar{x} and \bar{y} are the sample means. n is the sample size (length of \mathbf{x} or \mathbf{y}).

In our application, the element of the fiber morphological matrix is a feature vector. The definition in Eq. (5) was extended to hyper matrices. Similarly, we converted the upper triangular part of such a matrix to a vector format and the Pearson correlation coefficient was defined as follows:

$$r = \frac{\sum_{i=1}^n (\mathbf{x}_i - \bar{\mathbf{x}})(\mathbf{y}_i - \bar{\mathbf{y}})^T}{\sqrt{\sum_{i=1}^n (\mathbf{x}_i - \bar{\mathbf{x}})(\mathbf{x}_i - \bar{\mathbf{x}})^T} \sqrt{\sum_{i=1}^n (\mathbf{y}_i - \bar{\mathbf{y}})(\mathbf{y}_i - \bar{\mathbf{y}})^T}} \quad (6)$$

where \mathbf{x}_i and \mathbf{y}_i are the feature vector of the samples, and $\bar{\mathbf{x}}$ and $\bar{\mathbf{y}}$ are the mean feature vectors averaged over all samples.

4) Functional metrics

We applied a method based on group-wise dictionary learning and sparse representation (Liu et al., 2017) to each fMRI data set, respectively. In brief, all grayordinate-based fMRI signals of the i^{th} subject were organized as a signal matrix $\mathbf{S}_i \in \mathbb{R}^{t \times m}$. The top panel of Fig. 4 shows two example subjects and their corresponding signal matrices. The columns are fMRI signals extracted from m cortical surface vertices and t is the length of time points (see the

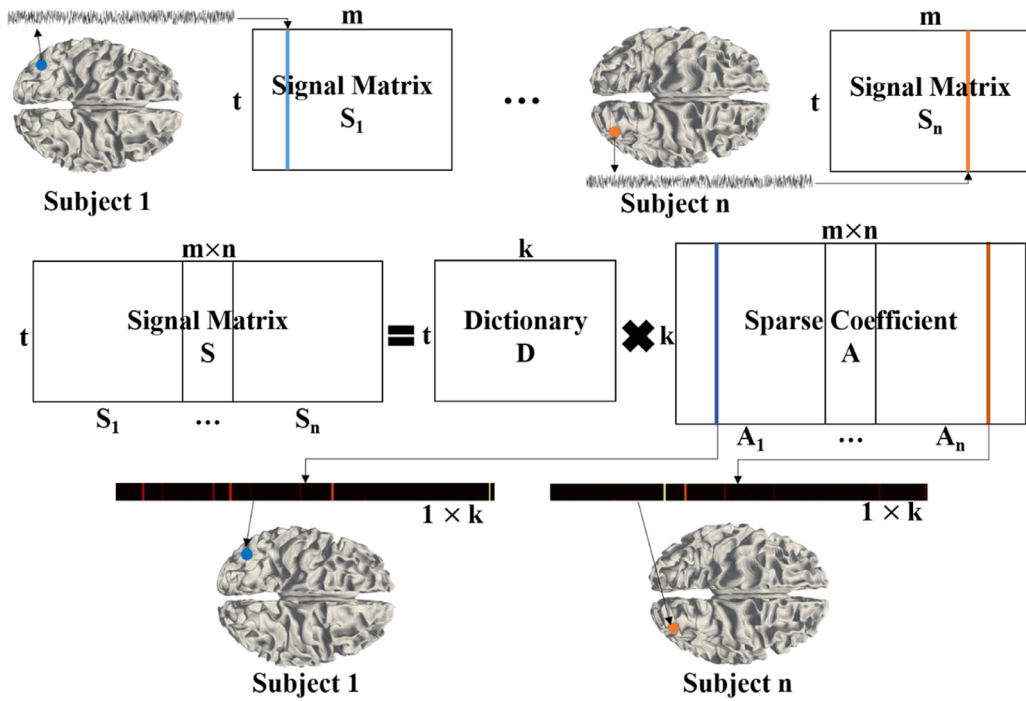


Fig. 4. Definitions of functional metrics. Details are referred to the texts.

example signals and how they are arranged as the columns). It is noted that m vertices were sampled on all subjects in the gray-coordinate system. After being normalized to zero mean and standard deviation, signal matrices of all subjects were concatenated as a multi-subject signal matrix $\mathbf{S} = [\mathbf{S}_1, \mathbf{S}_2, \dots, \mathbf{S}_n] \in \mathbb{R}^{t \times (m \times n)}$, where n is the number of subjects (the left matrix in the middle panel of Fig. 4). It is noted that every subject has m vertices on the gray-coordinate surface. The online dictionary leaning method in (Mairal et al., 2010) was applied to the multi-subject signal matrix \mathbf{S} to factorize it as $\mathbf{S} = \mathbf{D} \times \mathbf{A}$. $\mathbf{D} \in \mathbb{R}^{t \times k}$ is a group-wise temporal dictionary with k dictionary atoms ($k=400$ in this work). \mathbf{A} is a concatenated sparse coefficient weight matrix $\mathbf{A} = [\mathbf{A}_1, \mathbf{A}_2, \dots, \mathbf{A}_n] \in \mathbb{R}^{k \times (m \times n)}$, where $\mathbf{A}_n \in \mathbb{R}^{k \times m}$ corresponds to the n^{th} subject (the right matrix in the middle panel of Fig. 4). The m^{th} column of \mathbf{A}_n represents the weights of the k dictionary atoms that contribute to represent the original fMRI signal of the m^{th} vertex. Because the dictionary atoms in \mathbf{D} are shared by all subjects, columns of \mathbf{A}_n can be compared across subjects (the bottom panel of Fig. 4). See the blue and the orange bars in \mathbf{A}_n in Fig. 4, which are associated with the same two vertices in the top panel. Because all data modalities were in the same space (section 2.2), we identified the gray-coordinate vertices where the 3-hinges are located, and extracted their corresponding columns from \mathbf{A}_n s and used them as the 3-hinges' functional profiles. The 3-hinges that have cross-subject correspondences are expected to have similar functional profiles. The Euclidian distance between two functional profiles is used to measure their similarity. The functional similarity between two subjects is defined as the mean distance over all corresponding 3-hinge pairs. Vertices that find no correspondences (recall that the subject having more 3-hinges than the other subject usually have null correspondence for some 3-hinges) are not included in the functional similarity computation between a subject pair.

4) Manual Labeling

Because there are no "ground truth" on human brains, we manually identified the correspondence for 3-hinges on precentral gyrus and postcentral gyrus, because the morphology and topology of the two gyri are relatively simple and consistent across subjects

such that fewer manual labeling errors are introduced. The manual labeled correspondences were used as the "ground truth" to evaluate the performance of different methods. The manual correspondence (in the format of a vector) was compared with the algorithm derived one (a vector). Because different subjects give the vectors of different sizes, we used the longest vector as the template and stretched the other vectors to the same length by adding Non-match elements. Therefore, the correspondence vectors across the cohort comprise a correspondence matrix. This matrix was directly compared to the manual labeling correspondence matrix. The numbers of the same elements in two matrices, i.e., the number of matching correspondences on the cohort, were counted and divided by the total element number in a matrix. This overlapping ratio was used to measure the agreement of the estimated correspondence to the "ground truth".

2.8. Other Matching Methods for Comparisons

The first group of methods are the pair-wise graph matching method with a single view or two views, and the group-wise method with a single view. These comparisons aim to demonstrate the efficacy of two-view scheme and the group-wise scheme.

The second group of methods are volume-based (FSL-FNIRT, Andersson, et al., 2010) and surface-based (FreeSurfer, Fischl et al., 1999b) registration methods that use T1-weighted MRI data as inputs. It is worth noting that the two registration methods were performed in a "group-wise" manner. Taking FreeSurfer for example, In the first iteration, we used the standard template provided by the software, in order to eliminate the bias introduced by using any one subject as the template. To this template, individual surfaces were registered pair-wisely. Then, a custom template was yielded as an "average" surface of all registered surfaces. In the following iterations, the custom template was used to replace standard template and was updated. In each iteration, the warp fields were applied to 3-hinges' locations, such that 3-hinges from all subjects are in the same space. Like our graph matching algorithm, we used the subject that has the most 3-hinges as the reference. After the matching was completed, we computed the Euclidean

distance between all pairs of 3-hinges across two subjects. The Hungarian algorithm (Munkres, 1957) was applied to the distance matrix between two subjects to yield a one-to-one matching of 3-hinges. For a subject having fewer 3-hinges than the template, we randomly assigned null 3-hinges to the template's 3-hinges that have no matches. More details on this pipeline are referred to Supplemental Material I (section 1). The metrics introduced in section 2.7 were used as metrics in the comparisons between our method and other ones.

3. Results

3.1. Efficacy of Folding Topology and Fiber Morphological Features

Macaque brains have much fewer inter-individual variabilities in cortical folds. Numbers, locations and spatial distributions of their 3-hinges are relatively consistent across subjects (see the 8 randomly selected macaque white matter surfaces as well as their gyral nets and 3-hinges in Fig. 5(a)). By using the semi-automatic approach introduced in section 2.4, we identified 64 3-hinges as well as the gyral net on each macaque hemisphere. They were used as the “ground truth” to demonstrate that if the fiber morphological features and folding topological features within 3-hinges are consistent across subjects. This, in turn, demonstrates that it is reasonable to use those features to estimate cross-subject correspondences for 3-hinges on human brains.

Gyral nets and dMRI derived connective strength matrices within the 3-hinges system were derived from 8 randomly selected subjects and shown in Fig. 5(a)&(b).

The connective strength was defined as the number of deterministic streamline fibers that connect two 3-hinges (simultaneously pass through the 3mm neighborhoods of the two 3-hinges). They provide an intuitive impression on the cross-subject consistency in topological patterns of gyral nets (dashed curves) and fiber connective patterns. It is noted that we used fiber morphology feature in our algorithms, but it is difficult to be visualized in a 2D matrix format. We thus used the connective strength matrices instead to show the fiber consistency. We further quantified the consistency by computing the gyral net geodesic length matrix and the fiber morphology hyper matrix defined in section 2.5, and used Eqs. (5) & (6) to measure the similarity between a pair of matrices for each feature, respectively. The similarity rs of subject pairs were organized in a subject-matrix format (Fig. 5(c) shows the similarity among the eight example subjects). On average, the inter-individual similarity among all 18 subjects is 0.80 ± 0.13 for gyral net geodesic length matrix and 0.69 ± 0.07 for fiber morphology hyper matrix. To demonstrate that these similarity values are high and not produced by chance, we randomly selected 64 gyral nodes on each hemisphere and compute their geodesic length matrix and fiber morphological matrix. The average rs were computed. This random test was repeated 10,000 times to sample the null distribution (the null hypothesis is that the values of 0.80 ± 0.13 and 0.69 ± 0.07 are produced by chance). This null hypothesis was rejected by the results that very few of these random tests produced higher rs than 3-hinge systems ($p < 0.001$). These results demonstrate the cross-subject consistency of 3-hinges in terms of their fiber morphology and cortical folding topology. They also demonstrate that these two features can be used for 3-hinges' correspondence estimation on human brains.

We further evaluated the efficacy of fiber morphological feature by comparing it with connective strength feature and fiber length feature. The inter-individual similarity is 0.59 ± 0.09 and 0.56 ± 0.13 for the connective strength matrix and fiber length matrix (by Eqs. (5)), respectively, which are lower than that for the fiber morphological matrix (0.69 ± 0.07 as mentioned above).

We also compared the morphological feature, connective strength and fiber length by their performance in estimating 3-hinge correspondence. We applied the single-view-group-wise graph matching algorithm to estimate the cross-subject correspondence for 3-hinges (single-view was used because the effect of gyral net topology should be ruled out). The fiber morphological matrix, the connective strength matrix and fiber length matrix were used as the inputs to the single-view graph matching method, respectively. The cross-subject correspondences of 3-hinges determined by our automatic-plus-manual-checking method were used as the ground truth to evaluate the performance.

We computed the proportion of subjects that found the correct correspondence over all 3-hinges. The proportion is 67% (12 subjects) for fiber morphological feature, 44% (8 subjects) for the connective strength feature and 39% (7 subjects) for the fiber length.

We also measured the distance between the predicted 3-hinge and the ground-truth one, denoted by d . Because the 3-hinges are sparse on a macaque cortex and far away from each other, wrong assignment will produce large distance value. Therefore, we also computed the average distance between the 3-hinges within the 1st order and 2nd order neighborhoods in the entire gyral net system, denoted by d^1 and d^2 , respectively. Then, we used the ratio d/d^1 , and d/d^2 to measure the accuracy of the assignment. $d/d^1 > 1$ denotes that the predicted 3-hinge is far from the “ground truth” one than its 1st-order-neighbor range. On average, for the 1st order distance ratio d/d^1 , the accuracy is 2.46 ± 2.01 for connective strength, 2.23 ± 2.12 for fiber length and 1.38 ± 1.10 for fiber morphology. For d/d^2 , the accuracy is 1.31 ± 0.73 , 1.29 ± 1.13 , and 0.74 ± 0.49 , respectively. These results suggest that the fiber morphological matrix yields the best prediction of 3-hinge correspondence. A wrongly matched 3-hinge by fiber morphological matrix is near the 1st order neighbors of the ground-truth one but no further than its 2nd order neighbors. A possible reason is that the element of the connective strength/length matrix is a scalar while the element of the morphological matrix is a vector. An edge e_{ij}^P in subject P could be matched to many e_{ij}^Q 's in subject Q when a scale feature is used, because these e_{ij}^Q 's could have similar strength/length values. In this sense, a vector could potentially provide more discriminative information among those e_{ij}^Q 's.

In summary, fiber bundle morphology matrix is more consistent across subjects than connective strength/length matrix. The morphology matrix outperforms the others in estimating the cross-subject correspondence. Therefore, fiber bundle morphology was adopted in our work.

3.2. Effectiveness of the Two-view and the Group-wise Schemes

There are a couple of parameters in our algorithm to be determined. β (line 6 in Algorithm 1) and ε (line 9 in Algorithm 3) control the converging speed of the algorithm and work in a similar way, where larger β or ε makes the largest element in the vector closer to 1 while the others to 0. In our algorithm, they do not strongly affect the graph matching results, but small values will slow down the speed of convergence. Therefore, we empirically used 30 and 10 for β and ε , respectively. α (line 12 in Algorithm 1) controls the extent to which the two-way constraint is integrated. Similarly, it does not strongly affect the result but only the speed of convergence. We empirically used 0.3 for it. γ in line 7 in Algorithm 3 is the residual threshold of the group mean matrices M_s of two successive iterations, which is set to be 1×10^{-4} in our algorithm. The maximal iteration step δ is set to be 100. In our applications, the algorithm converges for all experiments using fewer iterations than 100.

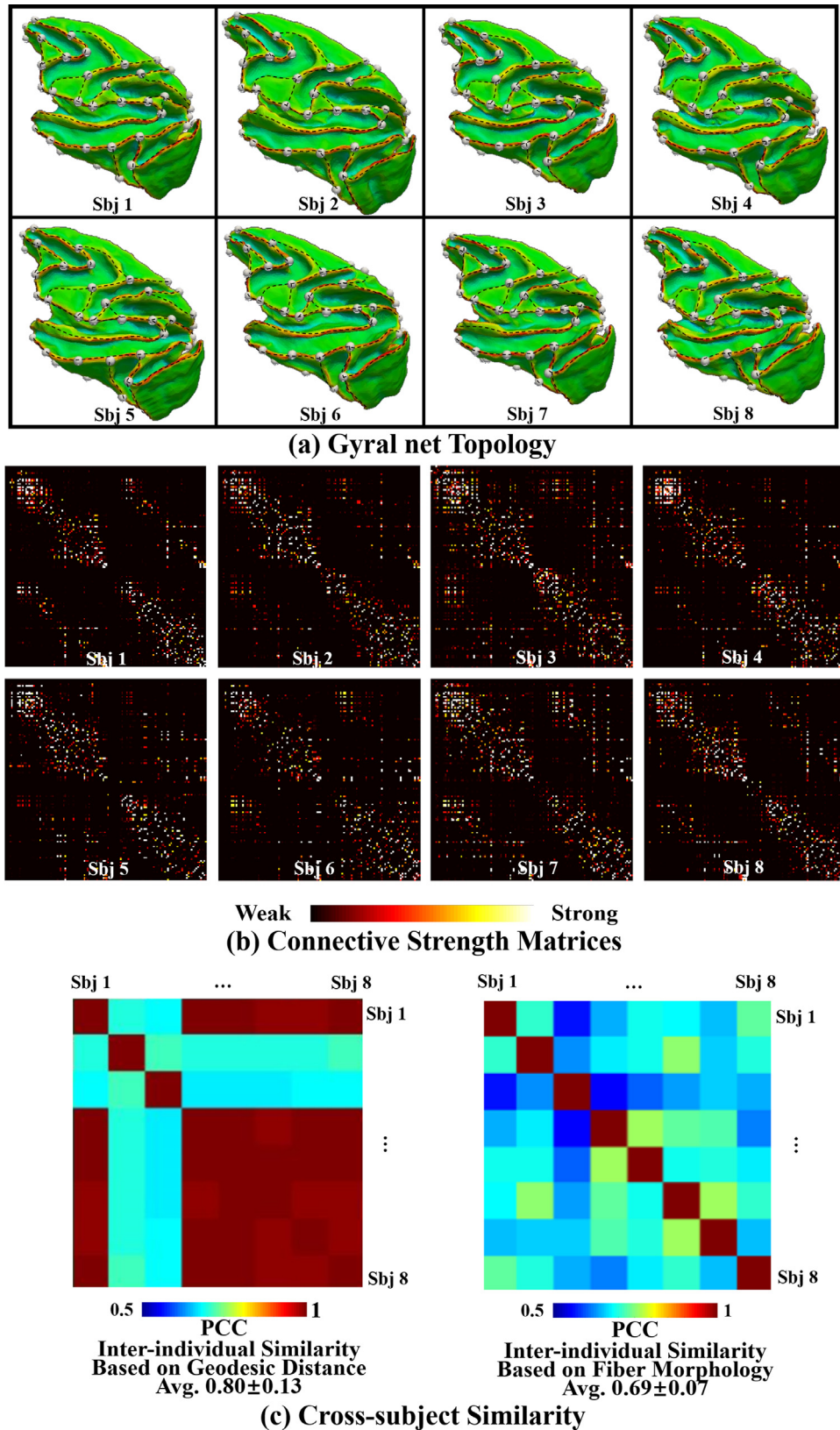


Fig. 5. (a) Dorsal view of macaque left hemisphere surfaces (color coded by curvature, red: positive curvature, blue: negative curvature), 3-hinges (white bubbles) and gyral nets (black dashed curves). The eight subjects were randomly selected. Due to the similarity between two hemispheres and for a better illustration of gyral net topology, only the left hemispheres were shown. (b) A connective strength matrix for each subject within the 3-hinge systems derived from dMRI data. (c) Left: Inter-individual similarity based on gyral net topological matrices. Right: Inter-individual similarity based on fiber morphology matrices. The similarity between a pair of matrices is defined as the Pearson correlation coefficient (Eqs. (5) & (6)). The subjects in (b) & (c) are the same eight macaques in (a).

Table 1

ICC used to evaluate the estimated 3-hinge correspondence for the cohort. S is short for single and T is short for two. Pair is short for pair-wise and group is short for group-wise.

S-view pair		S-view group		T-view pair	T-view group
Fiber	Gyral Net	Fiber	Gyral Net		
0.78	0.82	0.82	0.8626	0.84	0.8637

3.2.1. On Toy Models

In this section we evaluated the effectiveness of the two-view and the group-wise schemes in the limit as random graph edges and weights.

To evaluate the performance of two-view scheme, we only used the pair-wise graph matching (Algorithm 2), in order to remove the effect of the group-wise scheme. The two-view matching and the single-view matching were applied to the same set of random graphs, and the results were compared. The rows and columns of weight matrices as well as the “ground-truth” correspondence indices were shuffled and fed to the algorithm. The shuffled “ground-truth” indices were also recorded and denoted by \mathbf{x}_g . In general, the efficacy of the two-view scheme was demonstrated by its higher posterior inter-view terms $\mathbf{x}^T \mathbf{W}_1 \mathbf{y} + \mathbf{y}^T \mathbf{W}_2 \mathbf{x}$ (39.94 ± 5.91) and its total energy $E(\mathbf{x}, \mathbf{y})$ (79.65 ± 12.14) defined in Eq. (3) than single-view ones (24.09 ± 5.16 and 70.78 ± 12.07 for each single view, respectively).

To evaluate the performance of the group-wise scheme, we only used the single-view matching in order to remove the effects of that two-view scheme. The group-wise matching and the pair-wise matching were applied to the same set of random graphs, and the results were compared. It is noted that the 3-hinges’ indices as well as the columns and rows in the weight matrices were shifted in each iteration during the graph matching process. This shift was also applied to the “ground-truth” indices \mathbf{x}_g , accordingly. The final \mathbf{x}_g s are expected to be the same across subjects. We used ICC (introduced in section 2.7) on the final \mathbf{x}_g s of the entire cohort to measure their group-wise consistency. For the pair-wise scheme, we used one randomly selected subject as the template, to which another subject was matched. When all pair-wise matchings were performed, ICC was measured on the final \mathbf{x}_g s for all subjects. In general, the group-wise scheme outperforms the pair-wise scheme due to its higher r -value of ICC (0.21 ± 0.05 vs. 0.04 ± 0.02). It is noted that r -values are low because all graphs in toy models were randomly generated and the cross-subject consistency is intrinsically low. More details for toy model experiments are referred to the Supplemental Material I (section 3).

3.2.2. On Macaque Brains

Because 3-hinge correspondence on macaque were manually identified (Section 3.1), it can be used as the “ground truth” to evaluate the efficacy and precision of the two-view and the group-wise schemes in our methods. We used ICC to measure the consistency of estimated 3-hinge correspondence indices for the entire cohort.

It is seen in Table 1 that the two-view method outperforms either of the single-view method in both pair-wise comparisons (dark color columns) and group-wise comparisons (light color columns). Within single-view (blue columns) or two-view comparisons (gray columns), group-wise results outperform pair-wise ones. Improvements made by two-view methods are marginal compared to gyral-net-based single-view method (bold fonts). The reason could be that gyral nets of the macaque brains are consistent (Fig. 5(a)), such that the benefits brought by incorporating fiber morphological features may not be significant.

Table 2

The agreement between the correspondences from the ground truth and the algorithm.

	Our Method (Two views)	FreeSurfer	FSL	Our Method (Gyral net)
Precentral	0.60	0.57	0.55	0.55
Postcentral	0.63	0.59	0.55	0.57

3.2.3. 3-hinges Correspondences on Human Brains

Algorithm parameters are the same as those in the beginning of section 3.2. It is worth specifying that the computation time of the algorithm linearly grows with the number of subjects used as inputs, because only a pairwise graph matching is performed between each individual matrix and group mean in each iteration. For example, when we estimate the correspondence for m new subjects, the best way is combining the m subjects with the original n subjects. The computation time on these $m+n$ subjects is $(m+n)/n$ times of the one on n subjects. The algorithm costs around 30 hours on a typical desktop computer when applied to all 64 human subjects. Although there is a huge cross-subject variability on human brains, the algorithm still converges on the human group (more details are provided in section 4 in the Supplemental Material I).

We show the identified cross-subject correspondences of 3-hinges in Fig. 6. Eight subjects were randomly selected as examples. Hinges that find correspondence on most subjects were highlighted by a larger font size. It is observed that 3-hinges with identified correspondences have consistent locations. For example, 3-hinges #22 (yellow indices) and #190 (cyan indices) are found in the left lateral occipital cortex and the right V1 area, respectively, on all subjects. Other examples are as follows: 3-hinges #118, #136 and #139 are on the left precentral gyrus. 3-hinges #280, #287 and #275 are on the right postcentral gyrus. 3-hinges #251 and #252 are on the right supramarginal gyrus. 3-hinges #135, #152 and #147 are on the Broca area. Recalling that no strict spatial constraints were applied to the algorithms (except the hemisphere constraint), we find that the spatial topologies of these abovementioned 3-hinge chains (such as the precentral gyrus chain #118–#136–#139) are well preserved across subjects. This could be attributed to the matching effects of gyral net topology. Fiber bundles emanating from corresponding 3-hinges are consistent across subjects as well. This could be attributed to the matching effects of fiber morphological features. Fiber bundles from 3-hinges #22 and #190 are shown in the bottom panel of Fig. 6. Those from other consistent hinges of eight random subjects were shown in Supplemental Material II. It is also noted that some 3-hinges do have more than one connection (see the white bubbles in bottom panel of Fig. 6). Details on connection number distribution are found in Supplemental Material I (section 2).

We manually identified the correspondence for all 3-hinges on precentral gyrus and postcentral gyrus for all subjects. According to the definition in section 2.7, the matching/overlapping ratios between the “ground truth” correspondence and those estimated from algorithms are reported in Table 2.

It is seen that our methods yield a higher overlapping ratio for the entire cohort than the other two methods, suggesting that the correspondence from our method agrees better with the manual labeling results. It is noted that the two registration methods only used anatomical information as metrics. We thus compared them with our method with only the single view of the gyral net (anatomical topology). It is seen (the rightmost column) that gyral net tied with FSL and was slightly outperformed by FreeSurfer. This result suggests the importance of multimodal feature integration. An illustration of the comparison among different methods is found in Figure S2.

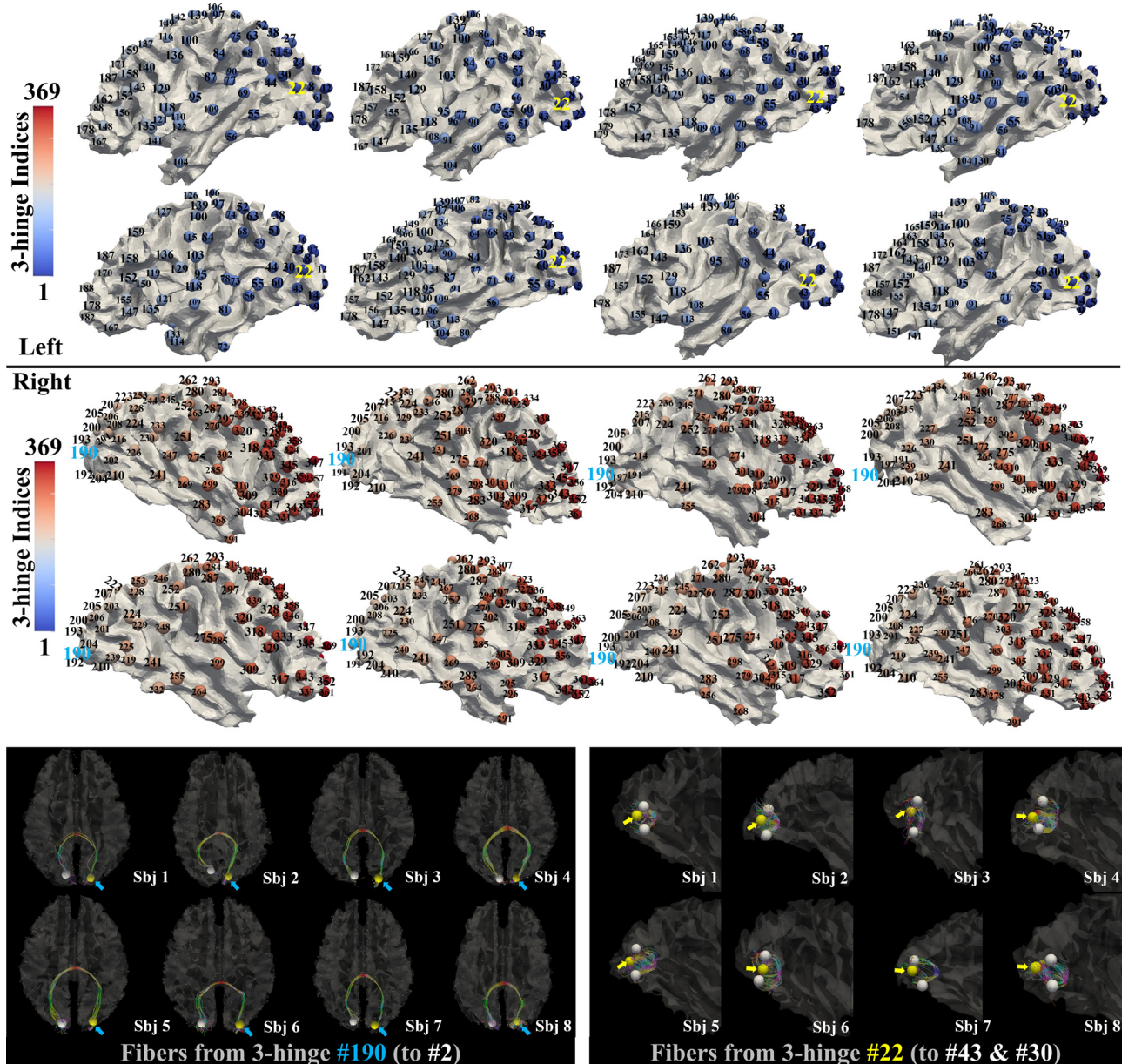


Fig. 6. 3-hinges with inter-individual correspondence on dorsal views of white matter surfaces. Eight subjects were randomly selected. Bubbles indicate the locations of 3-hinges and they are color-coded by correspondence indices, which are also indicated by numbers. Hinges that find correspondence on most subjects were highlighted by a larger font size. DMRI fibers emanating from 3-hinge #190 and #22 are shown in the bottom panel. Yellow/cyan indices or arrows highlight the locations of 3-hinges from which fibers were extracted. White bubbles highlight the locations of 3-hinges to which the fibers connect. It is noted that the surfaces derived from FA maps were used as the background for a better visualization purpose because they and the fibers are in the same space and there are no cross-modality registration errors.

3.3. Validation from fMRI Data

Unlike the manual labeling work in the previous section, it is difficult to manually label the “ground truth” for all 3-hinges’ correspondences on human brains. Instead, the structure-based results were evaluated by an independent functional metric. The functional similarity of the aligned 3-hinges for a pair of subjects was defined in section 2.7. The mean functional similarity (and the standard deviation) averaged over all subject pairs in the cohort is reported in Table 3. The functional similarity metrics were compared among approaches, including our proposed two-view matching method and single-view matching methods (fiber bundle morphology based or gyral net based), and imaging registration methods, such as FreeSurfer (Fischl et al., 1999b) and FSL-FNIRT (Andersson, et al., 2010). Both two-view matching and single-view

matching were performed under the group-wise scheme, because the superiority of this scheme over the pair-wise one has been demonstrated in section 3.2. The comparison between two-view and single-view in Table 3 is to emphasize the improvement by the joint use of both features. It is also worth reminding that inter-subject registrations via FSL-FNIRT and FreeSurfer were performed in a group-wise manner by creating a custom template (section 2.8 and Figure S1). The random assignment tests of 3-hinges correspondence were used to provide a baseline for the functional similarity metrics, which are also reported in the last column of Table 3 as a reference.

On average, our two-view & group-wise method produces the highest functional similarity for the cohort because of its lowest similarity metric values over all functional tasks. Low p -values (<0.05) of t -tests conducted between our method and another (in-

Table 3

Comparison of cohort consistency in terms of functional profiles within the aligned 3-hinges among different matching approaches. A smaller value indicates a higher consistency. The similarity was computed pair-wisely between subjects and the reported values are means \pm standard deviations averaged over all subject pairs. * indicates p -value of t -test is < 0.05 . *** indicates p -value of t -test is < 0.001 . The t -tests are between our method (two-view) and one of the other methods.

Tasks	Two-view ($\times 10^{-1}$)	Single-view ($\times 10^{-1}$)		FreeSurfer ($\times 10^{-1}$)	FNIRT ($\times 10^{-1}$)	Random
	Fiber	Gyral Net				
RST	1.56 \pm 0.46	4.06 \pm 1.46***	4.11 \pm 1.49***	1.76 \pm 0.52*	4.29 \pm 1.40***	4.55 \pm 0.39***
EMO	1.16 \pm 0.31	2.99 \pm 1.00***	3.01 \pm 1.02***	1.29 \pm 0.30*	3.06 \pm 1.05***	3.28 \pm 0.18***
GAM	1.17 \pm 0.36	3.02 \pm 1.11***	3.03 \pm 1.13***	1.30 \pm 0.37*	3.18 \pm 1.07***	3.35 \pm 0.35***
LAN	1.22 \pm 0.39	3.20 \pm 1.21***	3.22 \pm 1.22***	1.41 \pm 0.40*	3.35 \pm 1.13***	3.57 \pm 0.27***
MOT	1.33 \pm 0.39	3.49 \pm 1.23***	3.52 \pm 1.25**	1.48 \pm 0.40*	3.63 \pm 1.09***	3.84 \pm 0.38**
REL	1.22 \pm 0.35	3.16 \pm 1.11***	3.19 \pm 1.12***	1.33 \pm 0.38*	3.23 \pm 1.05***	3.48 \pm 0.24***
SOC	1.24 \pm 0.37	3.17 \pm 1.16***	3.20 \pm 1.18***	1.34 \pm 0.40*	3.30 \pm 1.11***	3.50 \pm 0.36***
WM	1.21 \pm 0.38	3.15 \pm 1.19***	3.17 \pm 1.20***	1.36 \pm 0.41*	3.28 \pm 1.13***	3.47 \pm 0.29***

cluding the baseline) demonstrate the significant improvement of our method.

4. Discussion

In this work, we proposed a two-view & group-wise approach to estimate cross-subject correspondences for a group of unique critical cortical landmarks (3-hinges).

In this approach, we produced a pseudo group-mean in each iteration instead of selecting a subject as a template. The selection of a template, in many cases, is subjective and could easily introduce bias to the brain alignment especially when inter-individual variabilities are huge. Different choices of templates could possibly lead to different alignment results for the entire cohort. Unlike the single-subject template approach, the pseudo group-wise mean template was objectively produced and updated in each iteration. A subject with a large variability to others is assigned a lower weight to ensure that the group-mean moves towards the center of the population. Therefore, the group-wise mean is supposed to be in the centroid of the distribution of the cohort as it is a weighted average of all subjects. The group-wise scheme has been widely and successfully applied to image registration method (Bhatia et al., 2004; Wu et al., 2011; O'Donnell et al., 2012). We transfer this concept to our graph-matching applications, and its effectiveness has been demonstrated in our work. However, its performance can still be improved in a variety of aspects. For example, the group-mean is simply a centroid measured on a Euclidean distance map among subjects. In fact, the data distribution can be far more complex than being linear. A careful investigation of the data distribution can greatly help produce a more suitable group-mean template that fits the manifold.

It has been demonstrated in previous works that each brain functional region has a unique structural connective fingerprint (Passingham et al., 2002). Structural connections are supposed to predict functional regions with high precision. In practice, however, intrinsic limitations of dMRI, such as low spatial resolutions, could weaken the functional predictive power of structural connections. On the other hand, cortical folding patterns have been demonstrated to have a poorer performance in predicting cortical regions of higher functions (Fischl et al., 2007). Therefore, a multimodal approach is likely to yield significant improvements in brain alignments (Robinson et al., 2013; Tardif et al., 2015; Glasser et al., 2016).

On macaque brains, the gyral net topology is more consistent across subjects than fiber morphology. The benefit brought by integrating the two features is not pronounced (see the marginal improvement in Table 1). Contrarily, the gyral net and fiber morphology variabilities are huge on human, and the improvements brought by the two-view scheme is significant (see the illustrative

examples in Figure S6). We show two examples to illustrate how a mismatch is produced by using only one-view, and “corrected” by the other view.

It is noteworthy that the features we adopted in this work are both in a system level. The hyper-matrix for fiber morphology encodes the organization of the white matter pathways (Chklovskii, et al., 2002; Kaiser and Hilgetag, 2006; van den Heuvel, et al., 2012;). Therefore, the fiber morphological feature reflects the constructive cost of the extrinsic white matter system within the 3-hinges. The anatomical matrix encodes the topology of the entire gyral net, which itself is a cortical pathway system (Khan et al., 2013; Chen et al., 2017). The geodesic distance on surface between two vertices measures the intrinsic cost between them. Therefore, the two matrices may exhibit two systems competing to construct the most efficient and effective neuron-to-neuron connections during the brain development. This competition might provide clues to why a joint use of the two systems can predict cortical areas with a higher precision. For example, when the intrinsic system within the cortex between two nodes are more efficient, their functional correlation might be affected more by the cortical system. More weights might thus be added to the gyral net geodesic matrix when our two-view scheme aligns these two nodes. Therefore, a deeper investigation of how the two systems impose impacts on each other may provide more interesting clues to the relation between brain structural architectures and brain functions, though much more multimodal and multiscale evidences are needed.

The aim of brain alignment is to find the functional correspondence across subjects. However, because brain functions are dynamic and variable, brain structure was usually used as the surrogate to alignment brain functional regions. This is based on an assumption that brain structure serve as the substrate of brain functions. In fact, the relation between brain structure and function has been studied at a macro-scale in previous studies (Fischl et al. 2007; Passingham et al. 2002). Folding patterns seem to be too variable in higher-order BA to predict their functions (Fischl et al. 2007). In our previous works, we showed that dMRI derived fibers could not always precisely predict the locations of activated loci from task functional MRI (Zhang et al., 2012). Therefore, brain structure could be more likely to provide a constraint, whereby variable functions can be generated by the same brain structural diagram. This hypothesis suggests a many-to-one mapping between brain functions and brain structure (Park and Friston, 2013), and partially explains the pronounced divergence between brain structure and function in higher cortex on human. The divergence was also revealed by the cross-subject consistency of 3-hinges' correspondence which appears to be regionalized. The 3-hinges with poorer cross-subject correspondence were usually found in higher-order cortical regions, such as parietal lobes, frontal lobes and infe-

rior temporal lobes (see the indices with a smaller font size in Fig. 6). From another perspective, individualized exposure to variable environment settings could impose their impact on developing human brains, making each individual unique and its behavior inconsistent and unpredictable. In contrast, the anatomy and structural wiring diagram of macaque brains are more consistent across subjects. This consistency could be related to their more predictable behaviors than human subjects.

Our long-term goal is to investigate and define a novel mapping between brain structure and function at a finer resolution. We expect that 3-hinges could be used as such finer gyral landmarks to improve the accuracy of brain alignment and the accuracy between brain structure and function. We further expected that 3-hinges provide an organizing framework for the gyrus system (Chen et al. 2017), as what was suggested for sulcal pits in Lohmann et al. 2007. Regarding the cortical folding morphology, 3-hinges seem like the counterparts of the sulcal pits, the deepest sulcal regions (Lohmann et al., 2007; Im et al., 2010; Im et al., 2011; McKay et al., 2013; Meng et al., 2014). For sulcal pits, it was found that spatial distribution of sulcal pits in major sulci is regular across subjects (Lohmann et al., 2007). The presence of some sulcal pits were shown to be related with intelligence (Im et al., 2011). The general spatial arrangement of the sulcal pits looks like chains that follow the alignment of the lateral ventricles. These sulcal pits were thus suggested to provide an organizing framework for human cortical folding. It was also suggested that sulcal pits are under closer genetic control than other cortical folding patterns (McKay et al., 2013). Because the arrangements of both sulcal pits and functional areas are encoded in the protomap (Rakic 1984), the sulcal pits were suggested to have closer and clearer relation to functional areas than other cortical folding patterns. This relation further implies important potential applications in deep-sulcal-landmark-based interindividual registration. In fact, the notion of "gyral net" has been proposed in Chen et al., 2017, where the gyral region was represented by the gyral crest curves, which compose a gyral network and the crossings of which are gyral hinges. Therefore, 3-hinges are the anchors of the gyral net in their anatomical appearance and possess unique importance in structural and functional connectivity. Given these findings on sulcal pits and the similarity between them and 3-hinges, we postulate that 3-hinges may be higher than other gyral cortex in their altitude. The highest 3-hinges may be regular across subjects and they may form chains that also follow the arrangement of lateral ventricle. Note that we treat all 3-hinges as equal regardless of their height difference in this work. The alignment accuracy could be improved by identifying the highest (and possibly the most regular) 3-hinges and aligning them first and propagating the alignment further to other lower and more variable 3-hinges. The 3-hinges and sulcal pits might interleave with each other and exhibit a pinpoint framework of the cortical folding. We also postulate that 3-hinges, like sulcal pits, might be under closer genetic control than other gyral cortex. For example, regional differences of expression levels of a family of DNA-associated proteins (e.g., Trnp1) were found in cortex of human fetuses in (Stahl et al., 2013; Borrell and Götz, 2014). Higher levels of Trnp1 expression result in tangential expansion while lower levels lead to a radial expansion. In the cellular level of this theory, radial expansion results from prosperity of basal radial glial (RG) cells and basal progenitors (BP). The prosperity could generate considerable migrating neurons to cortical plate to give rise to radially convex folds. In this sense, the expression levels of Trnp1 in these convex regions might not be homogeneously low. The lowest levels might lead to the most prosperous generation of BPs and basal RGs and the most pronounced radial expansion, probably giving rise to 3-hinges.

In addition to gyral and sulcal patterns, another folding pattern "pli de passage", gyrus buried in sulcal valleys, was suggested to

serve as a linkage between the gyral system and the sulcal system (Gratiolet, 1854; Cunningham and Horsley, 1892). Sulcal pits were suggested to provide a possibility to "decompose the global sulcal pattern into reproducible building blocks overcoming the interruptions of the main sulci" (Mangin, et al., 2019). In this sense, pli de passage is an annexant convolution that bridges gyral regions and sulcal regions, and a future framework that incorporates gyral hinges, sulcal pits and pli de passages could provide a novel organizing framework for the entire cortical system.

Finally, the specificities of 3-hinges, such as their higher dMRI derived fiber density, could result from the gyral bias effect due to the limitation of the dMRI technique. Gyral bias could make the detection of entrance of axonal pathways to gray matter less sensitive on the walls (between gyral crests and sulcal fundi) and sulci than on gyral crest, making the comparison between gyri and sulci less trustworthy in terms of their axonal wiring patterns. However, one of our recent works (Zhang et al., 2019) focused on the contrast between 3-hinges and other ordinary gyral crest, both of which could be less impacted by the gyral bias effects. In this relatively "fare" comparison, 3-hinges were still demonstrated to exhibit higher axonal connections, thicker cortex and could constitute a more pronounced core in the cortico-cortical connective network. In general, we should use care to investigate the specificities of 3-hinges, especially in their dMRI fiber connections.

In summary, we have defined a novel gyral folding pattern, termed a 3-hinge, in our previous works. This folding pattern is characterized by its unique and important structural and functional features, providing insight into the structure-function relation. In our preliminary result, we have also identified cross-subject and even cross-species correspondence for them. All these results make 3-hinges potential cortical landmarks that may improve the brain anatomy and function alignment. Therefore, this work focused on the alignment of these critical cortical landmarks, whereby we could extend it to the alignment of the whole cortical folding systems. The functional correspondences of the aligned 3-hinges have also been demonstrated in this work, further endorsing the potential use of the framework on datasets where functional MRI data is not available, such as datasets of brain diseases.

Declaration of Competing Interest

The authors declare that they have no known competing financial interests or personal relationships that could have appeared to influence the work reported in this paper.

CRediT authorship contribution statement

Tuo Zhang: Methodology, Conceptualization, Writing - original draft. **Ying Huang:** Formal analysis, Investigation. **Lin Zhao:** Formal analysis, Investigation. **Zhibin He:** Visualization. **Xi Jiang:** Writing - review & editing. **Lei Guo:** Supervision, Project administration. **Xiaoping Hu:** Resources, Writing - review & editing. **Tianming Liu:** Writing - review & editing, Conceptualization, Funding acquisition.

Acknowledgements

T Zhang was supported by National Natural Science Foundation of China [31671005, 31971288, and U1801265]. X Jiang was supported by National Natural Science Foundation of China [61703073 and 61976045]. L Guo was supported by National Natural Science Foundation of China [61936007]. T Liu was supported by National Institutes of Health [DA033393 and AG042599] and National Science Foundation [IIS-1149260, CBET-1302089, BCS-1439051 and DBI-1564736].

Supplementary materials

Supplementary material associated with this article can be found, in the online version, at doi:10.1016/j.media.2020.101700.

References

- Andersson, JLR, Jenkinson, M, Smith, S, 2010. Non-linear registration, aka spatial normalisation. FMRIB technical report TR07JA2.
- Andersson, JLR, Sotiroopoulos, SN, 2016. An integrated approach to correction for off-resonance effects and subject movement in diffusion MR imaging. Neuroimage 125, 1063–1078.
- Amunts, K, Malikovic, A, Mohlberg, H, Schormann, T, Zilles, K, 2000. Brodmann's areas 17 and 18 brought into stereotaxic space –where and how variable? Neuroimage 11, 66–84.
- Avants, BB, Tustison, N, Song, G, 2009. Advanced normalization tools (ANTS). Insight j 2, 1–35.
- Barch, DM, Burgess, GC, Harms, MP, Petersen, SE, Schlaggar, BL, Corbetta, M, Glasser, MF, Curtiss, S, Dixit, S, Feldt, C, Nolan, D, Bryant, E, Hartley, T, Footer, O, Bjork, JM, Poldrack, R, Smith, S, Johansen-Berg, H, Snyder, AZ, Van Essen, DC, 2013. Function in the human connectome: task-fMRI and individual differences in behavior. Neuroimage 80, 169–189.
- Bertrand, G, 2005. On topological watersheds. Journal of Mathematical Imaging and Vision 22 (2-3), 217–230.
- Bhatia, KK, Hajnal, JV, Puri, BK, Edwards, AD, Rueckert, D, 2004. Consistent group-wise non-rigid registration for atlas construction. 2004 2nd IEEE International Symposium on Biomedical Imaging: Nano to Macro 908–911.
- Borrell, V, Götz, M, 2014. Role of radial glial cells in cerebral cortex folding. Current opinion in neurobiology 27, 39–46.
- Chen, H, Li, Y, Ge, F, Li, G, Shen, D, Liu, T, 2017. Gyral net: A new representation of cortical folding organization. Medical Image Analysis 42, 14–25.
- Chklovskii, DB, Schikorski, T, Stevens, CF, 2002. Wiring optimization in cortical circuits. Neuron 34, 341–347.
- Cho, M, Lee, J, Lee, KM, 2010. Reweighted random walks for graph matching. In European Conference on Computer Vision. 492–505.
- Cunningham, DJ, Horsley, V, 1892. Contribution to the surface anatomy of the cerebral hemispheres. Royal Irish Academy, Dublin.
- Dale, AM, Fischl, B, Sereno, MI, 1999. Cortical surface-based analysis: I. Segmentation and surface reconstruction. Neuroimage 9, 179–194.
- Derrfuss, J, Mar, RA, 2009. Lost in localization: the need for a universal coordinate database. Neuroimage 48 (1), 1–7.
- Desai, R, Liebenthal, E, Possing, ET, Waldron, E, Binder, JR, 2005. Volumetric vs. surface-based alignment for localization of auditory cortex activation. NeuroImage 26 (4), 1019–1029.
- Epstein, JN, Casey, BJ, Tonev, ST, Davidson, M, Reiss, AL, Garrett, A, Hinshaw, SP, Greenhill, LL, Vitolo, A, Kotler, LA, Jarrett, MA, Spicer, J, 2007. Assessment and prevention of head motion during imaging of patients with attention deficit hyperactivity disorder. Psychiatry Research 155, 75–82.
- Fischl, B, Sereno, MI, Dale, AM, 1999a. Cortical surface-based analysis: II: Inflation, flattening, and a surfacebased coordinate system. NeuroImage 9 (2), 195–207.
- Fischl, B, Sereno, MI, Tootell, RB, Dale, AM, 1999b. High-resolution intersubject averaging and a coordinate system for the cortical surface. Human Brain Mapping 8 (4), 272–284.
- Fischl, B, Salat, DH, Busa, E, Albert, M, Dieterich, M, Haselgrove, C, van der Kouwe, AJW, Killiany, R, Kennedy, D, Klaveness, S, Montillo, A, Makris, N, Rosen, B, Dale, AM, 2002. Whole brain segmentation: automated labeling of neuroanatomical structures in the human brain. Neuron 33, 341–355.
- Fischl, B, Salat, DH, van der Kouwe, AJW, Makris, N, Segonne, F, Quinn, BT, Dale, AM, 2004. Sequence-independent segmentation of magnetic resonance images. Neuroimage 23, S69–S84.
- Fischl, B, Rajendran, N, Busa, E, Augustinack, J, Hinds, O, Yeo, BT, Mohlberg, H, Amunts, K, Zilles, K, 2007. Cortical folding patterns and predicting cytoarchitecture. Cerebral Cortex 18 (8), 1973–1980.
- Frost, MA, Goebel, R, 2012. Measuring structural-functional correspondence: spatial variability of specialised brain regions after macro-anatomical alignment. Neuroimage 59, 1369–1381.
- Ge, F, Li, X, Razavi, MJ, Chen, H, Zhang, T, Zhang, S, Guo, L, Hu, X, Wang, X, Liu, T, 2017. Denser growing fiber connections induce 3-hinge gyral folding. Cerebral Cortex 28 (3), 1064–1075.
- Gratiolet LP, 1854. On the Folding of Cortical Folding of the Human and Primates Brain. Paris, Bertrand (Fre).
- Glasser, MF, Van Essen, DC, 2011. Mapping human cortical areas in vivo based on myelin content as revealed by T1- and T2-weighted MRI. Journal of Neuroscience 31, 11597–11616.
- Glasser, MF, Sotiroopoulos, SN, Wilson, JA, Coalson, TS, Fischl, B, Andersson, JL, Xu, J, Jbabdi, S, Webster, M, Polimeni, JR, Van Essen, DC, Jenkinson, M, Consortium, WU-Minn HCP, 2013. The minimal preprocessing pipelines for the Human Connectome Project. Neuroimage 80, 105–124.
- Glasser, MF, Coalson, TS, Robinson, EC, Hacker, CD, Harwell, J, Yacoub, E, Ugurbil, K, Andersson, J, Beckmann, CF, Jenkinson, M, Smith, SM, Van Essen, DC, 2016. A multi-modal parcellation of human cerebral cortex. Nature 536 (7615), 171.
- Goebel, R, Esposito, F, Formisano, E, 2006. Analysis of functional image analysis contest (fiac) data with brainvoyager qx: From single-subject to cortically aligned group general linear model analysis and self-organizing group independent component analysis. Human Brain Mapping 27 (5), 392–401.
- Gold, S, Rangarajan, A, 1996. A graduated assignment algorithm for graph matching. IEEE Pattern Anal. Machine Intell. 18 (4), 377–388.
- Greve, DN, Fischl, B, 2009. Accurate and robust brain image alignment using boundary-based registration. Neuroimage 48 (1), 63–72.
- Hinds, OP, Rajendran, N, Polimeni, JR, Augustinack, JC, Wiggins, G, Wald, LL, Diana, RH, Potthast, A, Schwartz, EL, Fischl, B, 2008. Accurate prediction of V1 location from cortical folds in a surface coordinate system. NeuroImage 39 (4), 1585–1599.
- Im, K, Jo, HJ, Mangin, JF, Evans, AC, Kim, SI, Lee, JM, 2010. Spatial distribution of deep sulcal landmarks and hemispherical asymmetry on the cortical surface. Cereb. Cortex. 20, 602–611.
- Im, K, Choi, YY, Yang, JJ, Lee, KH, Kim, SI, Grant, PE, Lee, JM, 2011. The relationship between the presence of sulcal pits and intelligence in human brains. Neuroimage 55 (4), 1490–1496.
- Jenkinson, M, Bannister, P, Brady, JM, Smith, SM, 2002. Improved optimisation for the robust and accurate linear registration and motion correction of brain images. NeuroImage 17 (2), 825–841.
- Jenkinson, M, Beckmann, CF, Behrens, TEJ, Woolrich, MW, Smith, SM, 2012. Fsl. Neuroimage 62, 782–790.
- Jiang, X, Li, X, Lv, J, Zhang, T, Zhang, S, Guo, L, Liu, T, 2015. Sparse representation of HCP grayordinate data reveals novel functional architecture of cerebral cortex. Human Brain Mapping 36 (12), 5301–5319.
- Kaiser, M, Hilgetag, CC, 2006. Nonoptimal component placement, but short processing paths, due to long-distance projections in neural systems. PLoS Computational Biology 2 (7), e95.
- Khan, S, Gramfort, A, Shetty, NR, Kitzbichler, MG, Ganesan, S, Moran, JM, Lee, SM, Gabrieli, JDE, Tager-Flusberg, HB, Joseph, RM, Herbert, MR, Hämaläinen, MS, Kenet, T, 2013. Local and long-range functional connectivity is reduced in concert in autism spectrum disorders. Proceedings of the National Academy of Sciences 110, 3107–3112.
- Klein, A, Andersson, J, Ardekani, BA, Ashburner, J, Avants, B, Chiang, MC, Christensen, GE, Collins, DL, Gee, J, Hellier, P, Song, JH, Jenkinson, M, Lepage, C, Rueckert, D, Thompson, P, Vercauteren, T, Woods, RP, Mann, JJ, Parsey, RV, 2009. Evaluation of 14 nonlinear deformation algorithms applied to human brain MRI registration. Neuroimage 46, 786–802.
- Lancaster, JL, Tordesillas-Gutiérrez, D, Martinez, M, Salinas, F, Evans, A, Zilles, K, Mazziotta, JC, Fox, PT, 2007. Bias between MNI and Talairach coordinates analyzed using the ICBM-152 brain template. Human Brain Mapping 28 (11), 1194–1205.
- Li, X, Chen, H, Zhang, T, Yu, X, Jiang, X, Li, K, Li, L, Razavi, MJ, Wang, X, Hu, X, Han, J, Guo, L, Hu, X, Liu, T, 2017. Commonly preserved and species-specific gyral folding patterns across primate brains. Brain structure and function 222 (5), 2127–2141.
- Liu, H, Zhang, M, Hu, X, Ren, Y, Zhang, S, Han, J, Guo, L, Liu, T, 2017. FMRI data classification based on hybrid temporal and spatial sparse representation. Biomedical Imaging (ISBI 2017). IEEE 14th International Symposium on 2017, pp. 957–960.
- Lohmann, G, Von Cramon, DY, Colchester, AC, 2007. Deep sulcal landmarks provide an organizing framework for human cortical folding. Cerebral Cortex 18 (6), 1415–1420.
- Mairal, J, Bach, F, Ponce, J, Sapiro, G, 2010. Online learning for matrix factorization and sparse coding. Journal of Machine Learning Research 11, 19–60.
- Mangin, JF, Le Guen, Y, Labra, N, Grigis, A, Frouin, V, Guevara, M, Fischer, C, Rivière, D, Hopkins, WD, Régis, J, Sun, ZY, 2019. "Pis de passage. Deserve a Role in Models of the Cortical Folding Process. Brain topography 1–14.
- Mazziotta, J, Toga, A, Evans, A, Fox, P, Lancaster, J, Zilles, K, Woods, R, Paus, T, Simpson, G, Pike, B, Holmes, C, Collins, L, Thompson, P, MacDonald, D, Iacoboni, M, Schormann, T, Amunts, K, Palomero-Gallagher, N, Geyer, S, Parsons, L, Narr, K, Kabani, N, Gouhalier, GL, Boomsma, D, Cannon, T, Kawashima, R, Mazoyer, B, 2001. A probabilistic atlas and reference system for the human brain: International Consortium for Brain Mapping (ICBM). Philosophical Transactions of the Royal Society of London. Series B: Biological Sciences. 356 (1412), 1293–1322.
- McKay, DR, Kochunov, P, Cykowski, MD, Kent, JW, Laird, AR, Lancaster, JL, Blangero, J, Glahn, DC, Fox, PT, 2013. Sulcal depth-position profile is a genetically mediated neuroscientific trait: description and characterization in the central sulcus. Journal of Neuroscience 33 (39), 15618–15625.
- Meng, Y, Li, G, Lin, W, Gilmore, JH, Shen, D, 2014. Spatial distribution and longitudinal development of deep cortical sulcal landmarks in infants. Neuroimage 100, 206–218.
- Munkres, J, 1957. Algorithms for the assignment and transportation problems. Journal of the Society for Industrial and Applied Mathematics 5 (1), 32–38.
- O'Donnell, LJ, Wells, WM, Golby, AJ, Westin, CF, 2012. Unbiased groupwise registration of white matter tractography. International Conference on Medical Image Computing and Computer-Assisted Intervention 123–130.
- Passingham, RE, Stephan, KE, Kötter, R, 2002. The anatomical basis of functional localization in the cortex. Nature Reviews Neuroscience 3 (8), 606.
- Pantazis, D, Joshi, A, Jiang, J, Shattuck, DW, Bernstein, LE, Damasio, H, Leahy, RM, 2010. Comparison of landmark-based and automatic methods for cortical surface registration. Neuroimage 49 (3), 2479–2493.
- Park, HJ, Friston, K, 2013. Structural and functional brain networks: from connections to cognition. Science 342 (6158), 1238411.
- Petrović, A, Smith, SM, Menke, RA, Jenkinson, M, 2009. Methods for tractography-driven surface registration of brain structures. International Conference on Medical Image Computing and Computer-Assisted Intervention 705–712.
- Rakic, P, 1984. Experimental modification of gyral patterns. Cerebral dominance:

- the biological foundations. Harvard University Press, CambridgeMassachusetts, p. 179.
- Raschle, N., Zuk, J., Ortiz-Mantilla, S., Sliva, DD., Franceschi, A., Grant, PE., Benasich, AA., Gaab, N., 2012. Pediatric neuroimaging in early childhood and infancy: challenges and practical guidelines. *Annals of the New York Academy of Sciences* 1252, 43–50.
- Régis, J., Mangin, JF., Ochiai, T., Frouin, V., Rivière, D., Cachia, A., Tamura, M., Samson, Y., 2005. "Sulcal root" generic model: a hypothesis to overcome the variability of the human cortex folding patterns. *Neurologia Medico-Chirurgica* 45 (1), 1–17.
- Robinson, EC., Jbabdi, S., Andersson, J., Smith, S., Glasser, MF., Van Essen, DC., Burgess, G., Harms, MP., Barch, DM., Jenkinson, M., 2013. Multimodal surface matching: fast and generalisable cortical registration using discrete optimisation. *International Conference on Information Processing in Medical Imaging* 475–486.
- Shen, D., Davatzikos, C., 2002. HAMMER: hierarchical attribute matching mechanism for elastic registration. *IEEE Transactions on Medical Imaging* 21 (11), 1421–1439.
- Smith, SM., Andersson, J., Auerbach, Ej., Beckmann, CF., Bijsterbosch, J., Douaud, G., Duff, E., Feinberg, DA., Griffanti, L., Harms, MP., Kelly, M., Laumann, T., Miller, KL., Moeller, S., Petersen, S., Power, J., Salimi-Khorshidi, G., Snyder, AZ., Vu, A., Woolrich, MW., Xu, J., Yacoub, E., Ugurbil, K., Van Essen, DC., Glasser, MF., 2013. Resting-state fMRI in the Human Connectome Project. *Neuroimage* 80, 144–168.
- Stahl, R., Walcher, T., Romero, CDJ., Pilz, GA., Cappello, S., Irmiger, M., Sanz-Aquela, JM., Beckers, J., Blum, R., Borrelli, V., Götz, M., 2013. Trnp1 regulates expansion and folding of the mammalian cerebral cortex by control of radial glial fate. *Cell* 153 (3), 535–549.
- Talairach, J., Tournoux, P., 1988. Co-planar stereotaxic atlas of the human brain. Thieme, New York.
- Tardif, CL., Schäfer, A., Waehnert, M., Dinse, J., Turner, R., Bazin, PL., 2015. Multi-contrast multi-scale surface registration for improved alignment of cortical areas. *Neuroimage* 111, 107–122.
- Thompson, P., Toga, AW., 1996. A surface-based technique for warping three-dimensional images of the brain. *IEEE Transactions on Medical Imaging* 15 (4), 402–417.
- Van Artevelde, N., Formisano, E., Goebel, R., Blomert, L., 2004. Integration of letters and speech sounds in the human brain. *Neuron* 43, 271–282.
- Van Essen, DC., Drury, HA., Joshi, S., Miller, MI., 1998. Functional and structural mapping of human cerebral cortex: solutions are in the surfaces. *Proceedings of the National Academy of Sciences* 95 (3), 788–795.
- Van Essen, DC., 2004. Surface-based approaches to spatial localization and registration in primate cerebral cortex. *NeuroImage* 23 (Supplement 1), S97–S107.
- Van Essen, DC., 2005. A population-average, landmark- and surface-based (pals) atlas of human cerebral cortex. *NeuroImage* 28 (3), 635–662.
- Van Essen, DC., Glasser, MF., Dierker, DL., Harwell, J., 2011. Cortical parcellations of the macaque monkey analyzed on surface-based atlases. *Cerebral Cortex*: 22 (10), 2227–2240.
- van den Heuvel, MP., Kahn, RS., Goñi, J., Sporns, O., 2012. High-cost, high-capacity backbone for global brain communication. *Proceedings of the National Academy of Sciences* 109 (28), 11372–11377.
- Wu, G., Jia, H., Wang, Q., Shen, D., 2011. SharpMean: groupwise registration guided by sharp mean image and tree-based registration. *NeuroImage* 56 (4), 1968–1981.
- Yeh, FC., Wedeen, VJ., Tseng, WYI., 2010. Generalized q-sampling imaging. *IEEE Transactions on Medical Imaging* 29 (9), 1626–1635.
- Yeh, FC., Verstynen, TD., Wang, Y., Fernández-Miranda, JC., Tseng, WYI., 2013. Deterministic diffusion fiber tracking improved by quantitative anisotropy. *PloS One* 8 (11), e80713.
- Zilles, K., Armstrong, E., Moser, KH., Schleicher, A., Stephan, H., 1989. Gyration in the cerebral cortex of primates. *Brain, Behavior and Evolution* 34 (3), 143–150.
- Zhang, T., Guo, L., Li, K., Jing, C., Yin, Y., Zhu, D., Cui, G., Li, L., Liu, T., 2012. Predicting functional cortical ROIs via DTI-derived fiber shape models. *Cerebral cortex* 22 (4), 854–864.
- Zhang, T., Zhu, D., Jiang, X., Ge, B., Hu, X., Han, J., Guo, L., Liu, T., 2013. Predicting cortical ROIs via joint modeling of anatomical and connectional profiles. *Medical Image Analysis* 17 (6), 601–615.
- Zhang, T., Chen, H., Guo, L., Li, K., Li, L., Zhang, S., Shen, D., Hu, X., Liu, T., 2014. Characterization of U-shape streamline fibers: Methods and applications. *Medical Image Analysis* 18 (5), 795–807.
- Zhang, T., Chen, H., Razavi, MJ., Li, Y., Ge, F., Guo, L., Wang, X., Liu, T., 2018. Exploring 3-hinge gyral folding patterns among HCP Q3 868 human subjects. *Human Brain Mapping* 39 (10), 4134–4149.
- Zhang, T., Li, X., Ge, F., Zhang, S., Zhao, L., Liu, H., Huang, Y., Yang, J., Guo, L., Hu, X., Liu, T., 2019. Cortical 3-hinges could serve as hubs in cortico-cortical connective network. *Brain Imaging and Behavior* 1–18.